Article

Current Biology

Noradrenergic circuit control of non-REM sleep substates

Graphical abstract

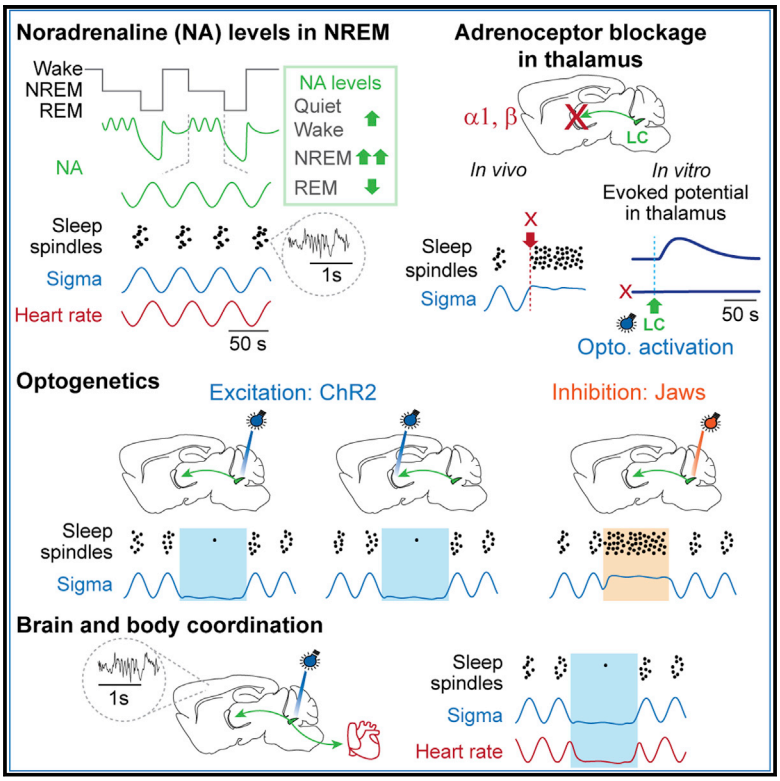

Highlights

- In NREMS, thalamic noradrenaline (NA) levels are higher than in quiet wakefulness
- Thalamic NA fluctuates over ~50 s and is anticorrelated to sleep spindles
- NA released from LC depolarizes thalamic neurons through α1- and β-adrenoceptors
- Infraslow LC activity coordinates heart-rate variations with spindles

Authors

Alejandro Osorio-Forero, Romain Cardis, Gil Vantomme, ..., Christiane Devenoges, Laura M.J. Fernandez, Anita Lüthi

Correspondence

anita.luthi@unil.ch

In brief

Osorio-Forero et al. find that the neurotransmitter noradrenaline, known to be released in attentive wakefulness, is also released during non-REM sleep. Noradrenaline levels reached are even higher than in quiet wakefulness and fluctuate to coordinate forebrain and autonomic correlates of arousability on a 50-s timescale.

Osorio-Forero et al., 2021, Current Biology *31*, 1–15
November 22, 2021 © 2021 The Author(s). Published by Elsevier Inc.
https://doi.org/10.1016/j.cub.2021.09.041

CellPress

Please cite this article in press as: Osorio-Forero et al., Noradrenergic circuit control of non-REM sleep substates, Current Biology (2021), https://doi.org/10.1016/j.cub.2021.09.041

Current Biology

CellPress
OPEN ACCESS

Article

Noradrenergic circuit control of non-REM sleep substates

Alejandro Osorio-Forero,[1] Romain Cardis,[1] Gil Vantomme,[1,2] Aurélie Guillaume-Gentil,[1] Georgia Katsioudi,[1,3] Christiane Devenoges,[1] Laura M.J. Fernandez,[1] and Anita Lüthi[1,4,5,*]

[1]Department of Fundamental Neurosciences, University of Lausanne, Rue du Bugnon 9, 1005 Lausanne, Switzerland
[2]Present address: Department of Neurology, Wu Tsai Neurosciences Institute, Stanford University, 290 Jane Stanford Way, Stanford, CA 94305, USA
[3]Present address: Center for Integrative Genomics, University of Lausanne, Génopode, 1015 Lausanne, Switzerland
[4]Twitter: @LabLuthi
[5]Lead contact
*Correspondence: anita.luthi@unil.ch
https://doi.org/10.1016/j.cub.2021.09.041

SUMMARY

To understand what makes sleep vulnerable in disease, it is useful to look at how wake-promoting mechanisms affect healthy sleep. Wake-promoting neuronal activity is inhibited during non-rapid-eye-movement sleep (NREMS). However, sensory vigilance persists in NREMS in animals and humans, suggesting that wake promotion could remain functional. Here, we demonstrate that consolidated mouse NREMS is a brain state with recurrent fluctuations of the wake-promoting neurotransmitter noradrenaline on the ~50-s timescale in the thalamus. These fluctuations occurred around mean noradrenaline levels greater than the ones of quiet wakefulness, while noradrenaline (NA) levels declined steeply in REMS. They coincided with a clustering of sleep spindle rhythms in the forebrain and with heart-rate variations, both of which are correlates of sensory arousability. We addressed the origins of these fluctuations by using closed-loop optogenetic locus coeruleus (LC) activation or inhibition timed to moments of low and high spindle activity during NREMS. We could suppress, lock, or entrain sleep-spindle clustering and heart-rate variations, suggesting that both fore- and hindbrain-projecting LC neurons show coordinated infraslow activity variations in natural NREMS. Noradrenergic modulation of thalamic, but not cortical, circuits was required for sleep-spindle clustering and involved NA release into primary sensory and reticular thalamic nuclei that activated both α1- and β-adrenergic receptors to cause slowly decaying membrane depolarizations. Noradrenergic signaling by LC constitutes a vigilance-promoting mechanism that renders mammalian NREMS vulnerable to disruption on the close-to-minute timescale through sustaining thalamocortical and autonomic sensory arousability.

INTRODUCTION

The restorative and beneficial effects of sleep arise from its continuity.[1] This requires that behavioral interactions with the sensory environment are suppressed. However, birds would crash and dolphins would drown if switching off from the sensory environment were not supplemented by vigilance.[2] Because natural dangers and predators pose a risk to all animals, irrespective of whether they are asleep or awake, it is natural to hypothesize that sleep evolution must have been tightly coupled to vigilance-promoting mechanisms. This may have placed natural healthy sleep dangerously close to vulnerability, such that minor shifts in the environment or in the organism's physiology easily disrupt sleep. Indeed, neurological and psychiatric conditions underlying sleep disorders are highly diverse, yet identifying their origins remains challenging.[3–5] For these reasons, a better estimate of sleep's vulnerability in the healthy animal and of its neuronal basis is desirable.

During deep, restorative non-rapid-eye-movement sleep (NREMS), the activity of wake-promoting areas projecting into the forebrain is much reduced.[6] However, already the first recordings of neuronal electrical activity in the sleeping animal indicated that not all these areas were entirely silent.[7–13] The locus coeruleus (LC), the most dorsal of ten noradrenergic nuclei located in the pontine brainstem,[14] is strongly wake promoting,[15,16] tonically active during wakefulness,[7,17] and becomes even more active in response to unexpected sensory stimuli.[17–19] The LC also remains active during NREMS, although at minor rates that do not cause awakening.[10,16,20,21] This LC activity coincides with electroencephalogram (EEG) rhythms, such as sleep spindles[10,21–23] and cortical slow waves,[20,24] and is relevant for sleep-dependent memory consolidation.[25] Opto- or chemogenetic reinforcement of LC activity in rodents lowers auditory arousal thresholds in NREMS[23] and increases functional connectivity in resting-state salience networks,[26] which is a signature of enhanced vigilance. Therefore, natural variations of LC activity during NREMS could underlie sleep's vulnerability. To address this, we aimed to elucidate the dynamics of LC noradrenergic activity and its functional impact on brain and bodily substates during NREMS. We used closed-loop optogenetic manipulation of LC activity in combination with local and global sleep recordings in mouse, fiber

This is an open access article under the CC BY license (http://creativecommons.org/licenses/by/4.0/).

Please cite this article in press as: Osorio-Forero et al., Noradrenergic circuit control of non-REM sleep substates, Current Biology (2021), https://doi.org/10.1016/j.cub.2021.09.041

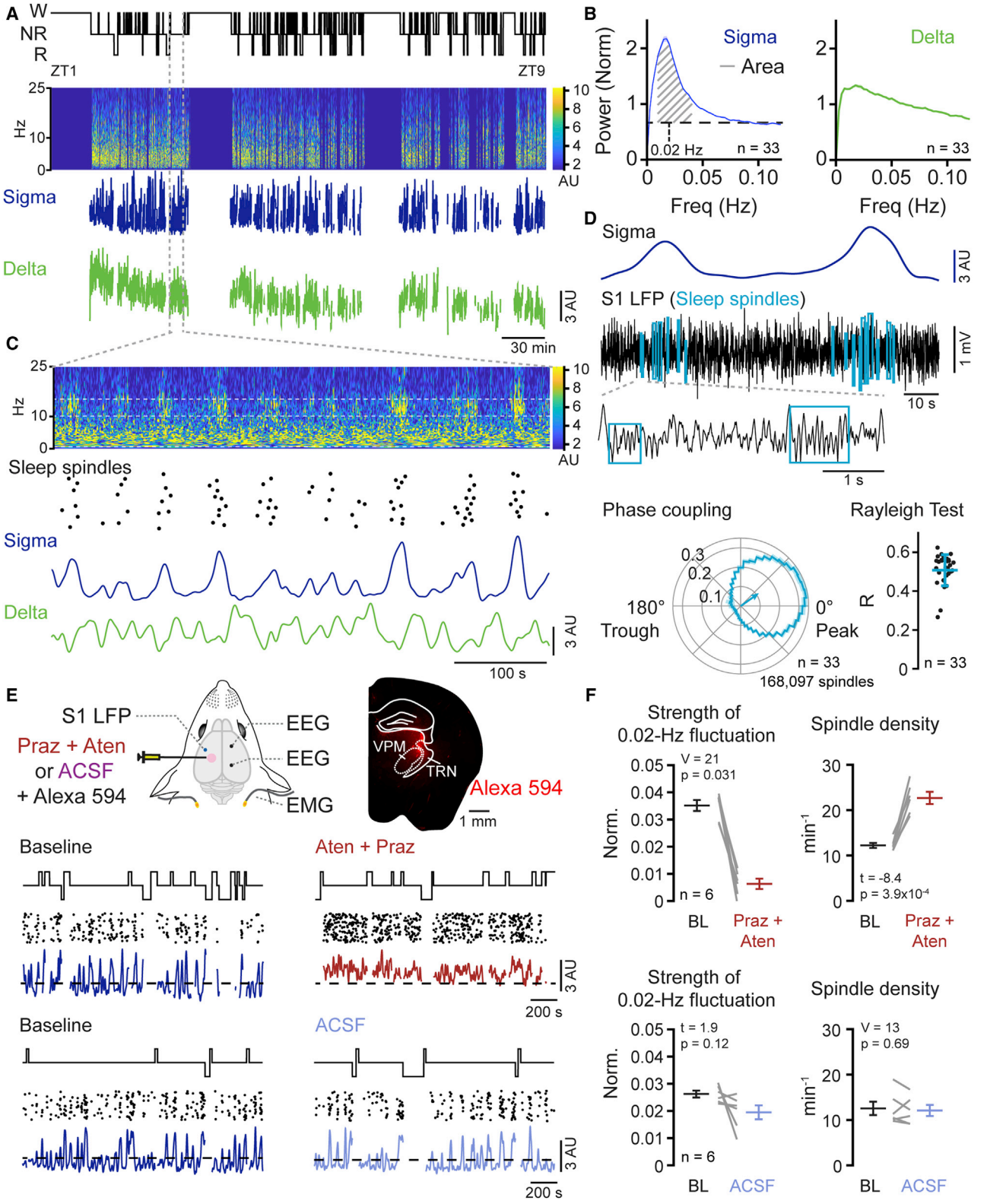

Figure 1. Noradrenergic signaling clusters sleep-spindle rhythms during NREMS

(A) Hypnogram showing wake (W), NREMS (NR), and REMS (R), with corresponding time-frequency distribution of S1 LFP signal. Power for NREMS in color code. Summed sigma (10–15 Hz) and delta (1.5–4 Hz) power dynamics were derived from the time-frequency distributions.

(legend continued on next page)

Please cite this article in press as: Osorio-Forero et al., Noradrenergic circuit control of non-REM sleep substates, Current Biology (2021), https://doi.org/10.1016/j.cub.2021.09.041

photometric assessment of noradrenaline (NA) levels, heart rate monitoring, and the analysis of synaptic potentials generated by LC afferents *in vitro*. We demonstrate that noradrenergic activity in thalamic sensory nuclei is unexpectedly high in NREMS and fluctuates on an infraslow timescale. Moreover, LC coordinates central and autonomic physiological correlates that make NREMS alternate between substates of low and high arousability.

RESULTS

Noradrenergic signaling during NREMS regulates the timing of sleep-spindle rhythms

Freely behaving mice sleep predominantly during the light period (ZT0–ZT12), which is their preferred resting phase. Figure 1A presents the sleep-wake behavior of a single mouse showing a hypnogram, obtained from polysomnography, and the corresponding time-frequency distribution derived from local field potential (LFP) recordings in the primary somatosensory cortex S1. We calculated power dynamics for two frequency bands characteristic for NREMS, the sigma (10–15 Hz) and the delta (1.5–4 Hz) frequency bands. As shown previously,[27,28] sigma power fluctuates prominently in S1 on an infraslow timescale with a peak ~50 s (~0.02 Hz; Figure 1B). This fluctuation underlies infraslow variations in spontaneous and sensory arousability.[27,28] Compared to sigma power, delta power in S1 fluctuates weakly (n = 33 mice; 12 C57BL/6J and 21 dopamine-β-hydroxylase [DBH]-Cre+/− mice recorded during the light phase; paired t test; t = 16.03; $p = 7.5 \times 10^{-15}$) and is anticorrelated to sigma in S1 due to shared neuronal mechanisms in local thalamocortical circuits.[29] The sigma frequency band is populated by sleep-spindle rhythms[30] that contribute to sensory decoupling during NREMS.[30,31] To determine whether sleep-spindle density covaried over 0.02 Hz, we used a previously developed spindle detection algorithm[29] (Figure S1A) and analyzed the phase-locking between sigma power and sleep spindle density in the same group of 33 mice, recorded during the light phase. Sleep spindles clustered at the peak of the 0.02-Hz fluctuation in sigma power, whereas they were rare in the troughs (Figures 1C and 1D). Polar plots depicting the phase coupling of 168,097 spindles to the 0.02-Hz fluctuation demonstrate the non-uniformity of this distribution (n = 33 mice; R of Rayleigh 0.51 ± 0.07; Figure 1D). Sleep spindles thus cluster on the 50-s timescale during NREMS, consistent with other reports in rodent and human.[32,33] This indicates that NREMS fluctuates between spindle-rich and spindle-poor substates that are now known to cause varying spontaneous and sensory arousability.[27,28,34]

To elucidate the role of noradrenergic signaling for infraslow variations in spindle density, we pharmacologically blocked noradrenergic receptors in thalamus, where sleep spindles originate.[30] C57BL/6J mice were injected with a mix of α1- and β-noradrenergic antagonists (0.1 mM prazosin hydrochloride and 5 mM (S)-(−)-atenolol; 150 nL) or control artificial cerebrospinal fluid (ACSF) (150 nL) locally into the somatosensory thalamus (Figure 1E). Exposure to these antagonists preserved the properties of individual spindles (Figure S1B). However, noradrenergic antagonist, but not ACSF injections, resulted in a rapid and reversible reduction of the strength of the 0.02-Hz fluctuation in sigma power in the ipsilateral S1 LFP, but not in the contralateral EEG (Figures 1E, 1F, and S2). Moreover, instead of being clustered, sleep spindles now appeared irregularly and at a mean density that was ~2-fold higher (Figure 1F). Noradrenergic signaling in thalamus appears thus necessary for the generation of spindle-free periods and their repeated clustering on the infraslow timescale.

Activity of the LC is necessary and sufficient for spindle clustering during NREMS

To optogenetically interfere with the activity of the noradrenergic LC during NREMS in a time-controlled manner, we virally infected LC neurons of DBH-Cre mice[35] to express excitatory (hChR2(H134R)_mCherry [ChR2_mCherry]) or inhibitory (Jaws_EGFP) opsins. Using immunohistochemistry for tyrosine hydroxylase (TH) in a subgroup of 4 animals, we found that ~80% of TH-positive cells expressed the viral transgene (Figure S3). We then implanted these animals with EEG/electromyogram (EMG), an S1 LFP electrode and an optic fiber positioned uni- (for ChR2-expressing animals) or bilaterally (for Jaws-expressing animals) over the LC (Figures 2A and 2B). Optimal fiber positioning was ensured through intra-surgical pupil diameter monitoring (Figure S4) and through post hoc anatomical verification (Figure S3). Using closed-loop monitoring of vigilance states, we first stimulated the LC specifically during NREMS at a low frequency (1 Hz; Figure 2C) and confirmed the successful expression of the opsins postmortem (Figures 2D and S3). The 1-Hz frequency is within the range of spontaneous LC unit activity during NREMS[20,21,36] and does not cause arousal in optogenetic studies.[16,21] Stimulation sessions took place in the first 20 min of each hour during 8 h of the light phase (ZT1–ZT9), with light or sham (light source turned off) stimulation alternating over successive recording days. Light stimulation in NREMS produced a rapid and almost complete suppression of sigma power and of sleep spindles. The effect lasted as long as light was present and instantly

(B) Fourier transform over sigma and delta power dynamics. Lines show means ± standard error (shadowed). Diagonal lines, area underneath the Fourier transform used to quantify the strength of the 0.02-Hz fluctuation; horizontal dashed line, mean values from 0.08 to 0.12 Hz.
(C) Single NREMS bout indicated in (A). Vertically jittered dots, automatically detected spindle events. See also Figure S1.
(D) Example S1 LFP raw trace showing automatically identified sleep spindles (Figure S1). "Phase coupling," sleep spindle occurrence along the 0.02-Hz fluctuation phases; arrow, mean Rayleigh vector; "Rayleigh test," quantification of the non-uniform distribution via R values ($p < 1.0 \times 10^{-16}$). Means ± standard errors are superimposed over individual datapoints. See also Figure S2.
(E) Scheme for intracranial local pharmacology and sleep recordings (STAR Methods). Prazosin hydrochloride (Praz) (0.1 mM) and (S)-(−)-atenolol (Aten) (5 mM) or artificial cerebrospinal fluid (ACSF) were co-injected with the red fluorescent dye Alexa Fluor 594 for post hoc verification. TRN, thalamic reticular nucleus; VPM, ventroposterior medial thalamus. Traces indicate hypnogram, sleep spindles, and sigma power for two representative mice injected either with Aten + Praz (top) or ACSF (bottom). Dashed horizontal line, mean sigma power in baseline.
(F) Strength of the 0.02-Hz oscillation (as explained in B) and of sleep-spindle densities for intracranial pharmacology experiments. Gray lines show individual animals; black, red, and blue lines show means ± standard error.

Please cite this article in press as: Osorio-Forero et al., Noradrenergic circuit control of non-REM sleep substates, Current Biology (2021), https://doi.org/10.1016/j.cub.2021.09.041

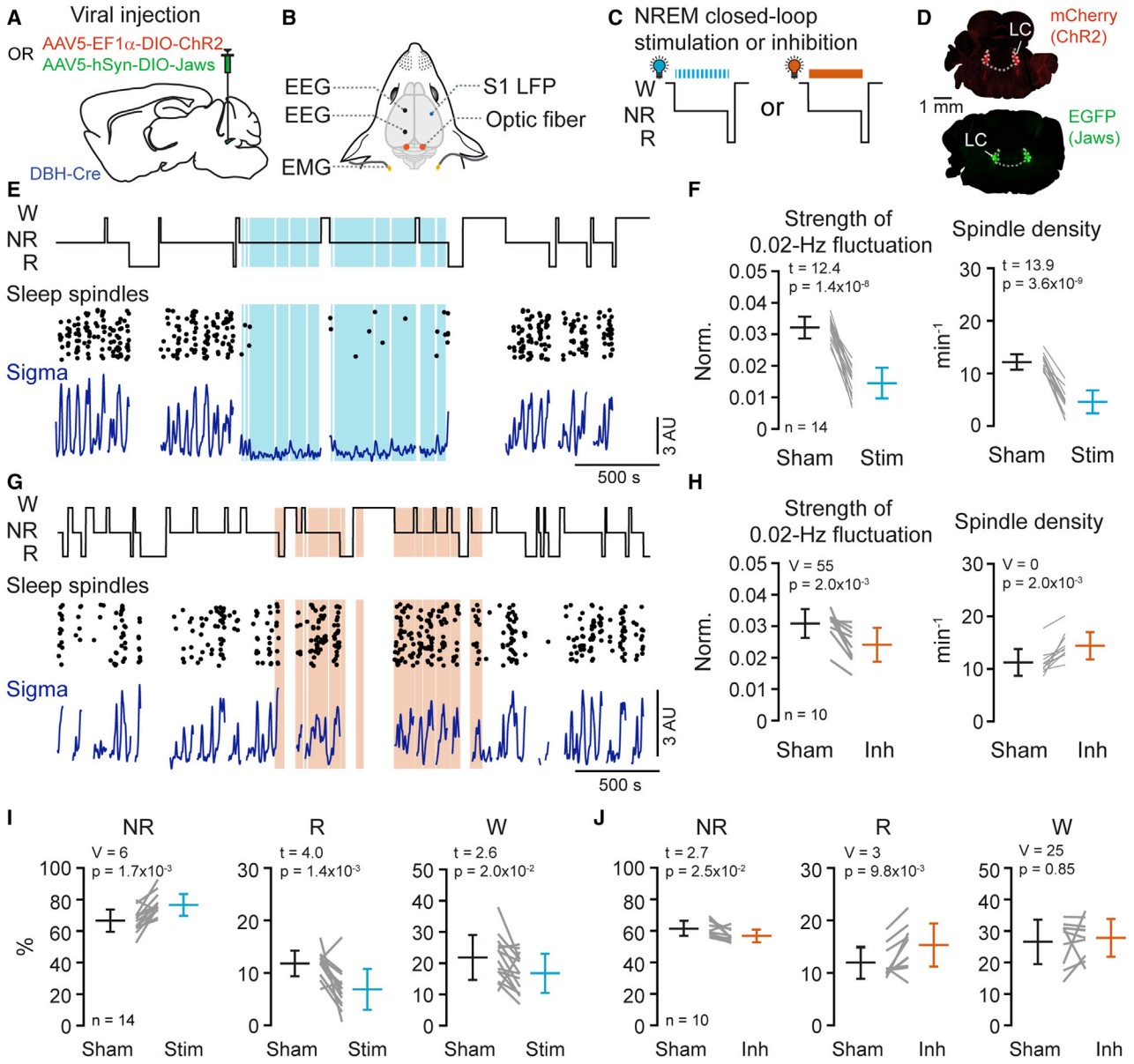

Figure 2. Optogenetic interrogation of the LC during NREMS

(A) Viral injection strategy for DBH-Cre mice.

(B) Experimental schematic showing electrode and fiber positioning.

(C) Schematic indicating closed-loop stimulation (blue) or inhibition (orange) of LC during NR.

(D) Representative fluorescent micrographs for two mice included in the dataset. See also Figure S3.

(E) Representative recording for optogenetic LC stimulation (1 Hz; blue shading) during NR, arranged as in Figure 1E. See also Figure S4.

(F) Quantification of effects on 0.02-Hz fluctuation strength and on spindle density. Gray lines show individual animals; black and blue lines show means ± standard error.

(G and H) Same as (E) and (F) for optogenetic inhibition of LC. Note that optogenetic inhibition was carried out almost exclusively during online detection of NREMS.

(I and J) Quantification of times spent in NR, R, or W during LC stimulation (I) or inhibition (J) and sham periods.

recovered once optogenetic stimulation stopped (Figure 2E), decreasing the strength of the 0.02-Hz fluctuation and sleep-spindle density (Figure 2F). These effects were not mediated directly by light or by light-induced heat propagation into LC, as verified via a computational model of heat propagation[37] and in control animals expressing mCherry alone (Figure S4). Conversely, continuous optogenetic inhibition according to the same experimental protocol locked sigma power at high levels and disrupted its fluctuation, increasing spindle density (Figures 2G and 2H). These results demonstrate that LC activity is both necessary and sufficient for the 0.02-Hz fluctuation and the clustering of sleep spindles.

Please cite this article in press as: Osorio-Forero et al., Noradrenergic circuit control of non-REM sleep substates, Current Biology (2021), https://doi.org/10.1016/j.cub.2021.09.041

CellPress
OPEN ACCESS

To explore whether LC stimulation or inhibition affected sleep architecture, we quantified total time spent in the different vigilance states. We found that LC stimulation prolonged total time spent in NREMS at the expense of REMS and wakefulness (Figure 2I), whereas LC inhibition had opposite effects (Figure 2J). These architectural alterations were not accompanied by significant changes in relative delta power in S1 (stimulation: increase by 7%, $t = -1.69$, $p = 0.11$; inhibition: decrease <1%, $t = -1.33$, $p = 0.90$). Therefore, a low level of LC activity appears to consolidate NREMS. This could be explained by an inhibitory action of monoaminergic signaling to enter REMS, which would cause NREMS to continue while we stimulated LC.[10,22,38]

LC signaling in thalamus, but not in cortex, underlies sleep-spindle clustering

From their thalamic site of origin, sleep-spindle activity propagates to cortical circuits.[30] As LC innervates both thalamic and cortical brain areas,[18,39] we tested the involvement of both innervation sites in the effects observed by direct LC stimulation. We placed the optic fiber over somatosensory thalamus or S1. For S1, the optic fiber stub was glued to the S1 LFP electrode at a distance of 800–1,200 μm over the tip (n = 5 mice) or inserted into layers 2/3, with the S1 electrode implanted below at an angle of 40° (n = 3 mice; Figures 3A and 3B). Confocal imaging demonstrated the presence of ChR2-expressing noradrenergic fibers in both thalamus and cortex (Figure 3C). Light stimulation of thalamic LC fibers reproduced the suppressive effects observed with direct LC stimulation (Figures 3D and 3E). In contrast, cortical stimulation was ineffective, irrespective of whether the optic fiber was positioned over the cortex or inserted into layer 2/3 (Figures 3F and 3G). This finding suggests that LC fibers targeting upper or lower cortical layers did not play a major role in regulating LFP correlates of sigma activity in S1. Note that all 8 animals implanted with an optic fiber over the cortex responded to direct optogenetic LC stimulation and are included in the data in Figure 2F. Thus, synaptic noradrenergic activity within the thalamus, but not the cortex, appears to sensitively control the clustering of sleep spindles measured in S1, in agreement with the pharmacological results in Figure 1.

LC activity fluctuates on an infraslow timescale during NREMS

LC cells can discharge action potentials in both tonic and phasic modes during wakefulness, and both these modes have also been proposed to occur during NREMS.[10,20,22,36] To address whether time variations in LC activity were relevant for the infraslow clustering of sleep spindles, we restricted the optogenetic manipulation of LC activity to distinct phases of the infraslow cycles. We detected these phases online through a machine-learning algorithm and triggered optogenetic activation based on whether sigma power started to rise or decline, thereby targeting preferentially high or low arousability periods (Figure 4).[28] When we optogenetically activated LC whenever sigma power started rising, the 0.02-Hz fluctuation was suppressed (Figures 4A and 4B). This indicates that sigma increases, and sleep-spindle generation, are not compatible with LC activity. Conversely, when we inhibited LC during sigma power decline, sleep-spindle density persisted at high levels (Figures 4C and 4D). The decline in sigma power thus required LC activity. These two results are best compatible with LC activity increasing on infraslow timescales to suppress sleep spindles.

Based on this result, we predicted that the converse experiment, stimulating LC when sigma power declined or inhibiting it when sigma power rose, would not disrupt infraslow dynamics. Intriguingly, for the first condition, successive cycles of high sigma power kept appearing (Figure 4E). Close inspection revealed that cycles appeared at shorter time intervals (sham: 52.9 ± 0.7 s; stim: 44.6 ± 1.7 s; n = 9; $p = 5.0 \times 10^{-7}$; paired t test) and were more regular, as evident by the decreased peak-to-peak variability (Figure 4F). Strengthening LC activity when it was already naturally high thus entrained a regular and faster infraslow fluctuation. When we specifically inhibited LC activity during online detected periods of low sigma activity, an entrainment was again observed, with interpeak intervals shortened (sham: 53.7 ± 2.6, inhibition: 50.8 ± 1.5 s, n = 9; paired t test, $p = 3.6 \times 10^{-3}$; Figure 4G) and regularized (Figure 4H). LC activity, already low at this moment, could thus be further inhibited by the light. This indicates that enforcing LC silence facilitates sigma level buildup and regularizes spindle clustering. Together, these results unravel a functionally relevant LC activity pattern during NREMS that interchanges between high and low activity at infraslow timescales.

Thalamic NA levels during NREMS are high and fluctuate on infraslow time intervals

LC activity is expected to increase NA within thalamus and to stimulate noradrenergic receptors. However, the time course of free NA is unknown, leaving open causal relationships to sleep-spindle dynamics. We used fiber photometry to measure free NA levels in somatosensory thalamus across the sleep-wake cycle by expressing the newly developed fluorescent NA biosensors $GRAB_{NE1h}$ or $GRAB_{NE1m}$ that have high and moderate affinity for NA, respectively.[40] Mice expressing one of the two biosensors in thalamus were implanted for sleep monitoring and fiber photometry. The fluorescence signals varied across the three vigilance states, declining in particular during REMS, similar to recent measures based on GRAB sensors in prefrontal cortex (Figure 5A).[22] We were surprised to see that NA levels during NREMS overlapped with the ones of quiet wakefulness within the first hours of the light phase, overall yielding higher mean values (Figures 5B and S5). We further observed rapid increases in NA levels when we stimulated the awake mouse in its cage by approaching one of our hands (Figure S6), indicating that thalamic NA levels followed variations in arousal during wakefulness. Focusing on NREMS bouts only, NA signals fluctuated in a manner inversely correlated with sigma power (with a time lag <0.5 s; $t = -1.0$; $p = 0.35$) and displaying recurrent negative peaks at infraslow intervals (Figure 5C). To resolve the time course of noradrenergic signaling on a cycle-to-cycle basis, we detected all infraslow sigma power cycles taking place during NREMS (excluding transitional periods) and examined the corresponding dynamics of free NA (Figure 5D). NA levels rose rapidly before sigma power declined, consistent with the suppressant effects of LC activity. Conversely, NA levels declined as sigma power was rising. Across animals, NA had already declined when sigma levels started rising, producing a non-symmetrical U-shaped time course. A similar profile of NA dynamics and similarly higher mean NA levels for NREMS compared to quiet

Please cite this article in press as: Osorio-Forero et al., Noradrenergic circuit control of non-REM sleep substates, Current Biology (2021), https://doi.org/10.1016/j.cub.2021.09.041

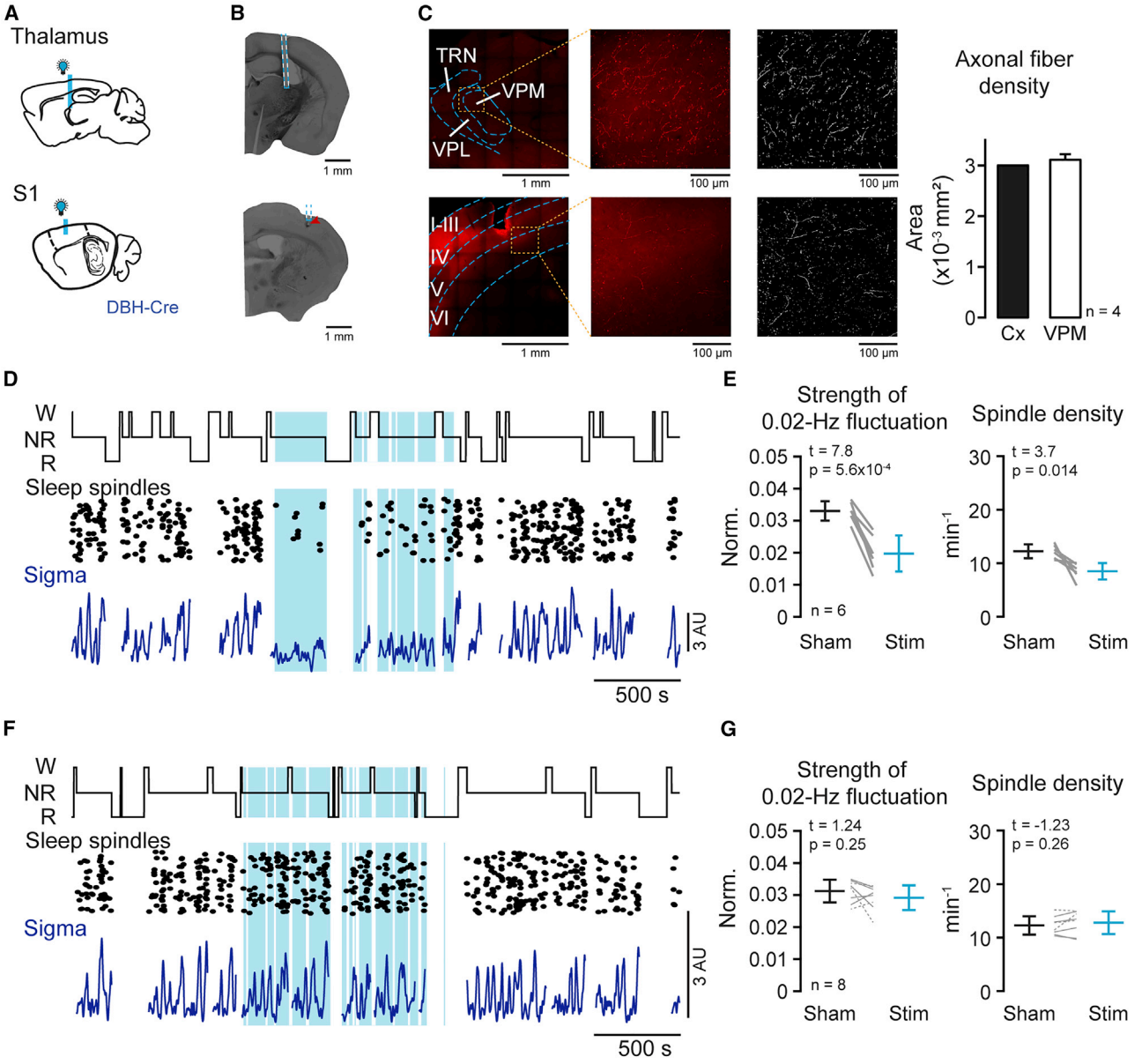

Figure 3. Optogenetic interrogation of LC afferents in thalamus or cortex during NREMS

(A) Experimental schematic indicating optic fiber positioning over somatosensory thalamus (VPM, top) or cortex (S1, bottom).

(B) Example anatomical verification of optic fiber locations (dotted lines). Red arrowhead, tip of LFP electrode. See also Figure S3.

(C) Representative images of noradrenergic LC fiber density within the thalamus (top) and S1 cortex (bottom). From left to right, full region of interest, selected area for quantification, and binary mask used for analysis (STAR Methods). Bar graphs, total area covered by bright pixels in a 0.13 mm^2 square. Data are means ± standard error.

(D) Representative traces for optogenetic stimulation of thalamic LC fiber terminals during NREMS; similar arrangement as in Figure 2E. See also Figure S4.

(E) Corresponding quantification of effects on 0.02-Hz fluctuation strength and on spindle density. Data presented as in Figure 2F.

(F and G) Same layout for experimental results in which the optogenetic fiber was positioned over cortex. Dotted lines, data from 3 animals with optic fiber positioned within layers 2/3.

wakefulness were observed for the medium-affinity biosensor $GRAB_{NE1m}$ (Figure S6), indicating that the natural dynamics of NA across vigilance states were detectable even for a >10-fold lower sensor affinity.[40] Therefore, noradrenergic signaling in thalamic sensory nuclei is higher than in quiet wakefulness during the resting phase and tightly matches the infraslow dynamics of sleep spindles.

Ionic mechanisms underlying NA-induced membrane depolarizations

When exposed to NA, thalamic cells *in vitro* depolarize such that they no longer engage in spindle-like rhythms.[41] However, the properties of LC-evoked postsynaptic potentials are unknown. We hence combined patch-clamp recordings with optogenetic LC fiber stimulation and studied evoked responses in

Please cite this article in press as: Osorio-Forero et al., Noradrenergic circuit control of non-REM sleep substates, Current Biology (2021), https://doi.org/10.1016/j.cub.2021.09.041

CellPress
OPEN ACCESS

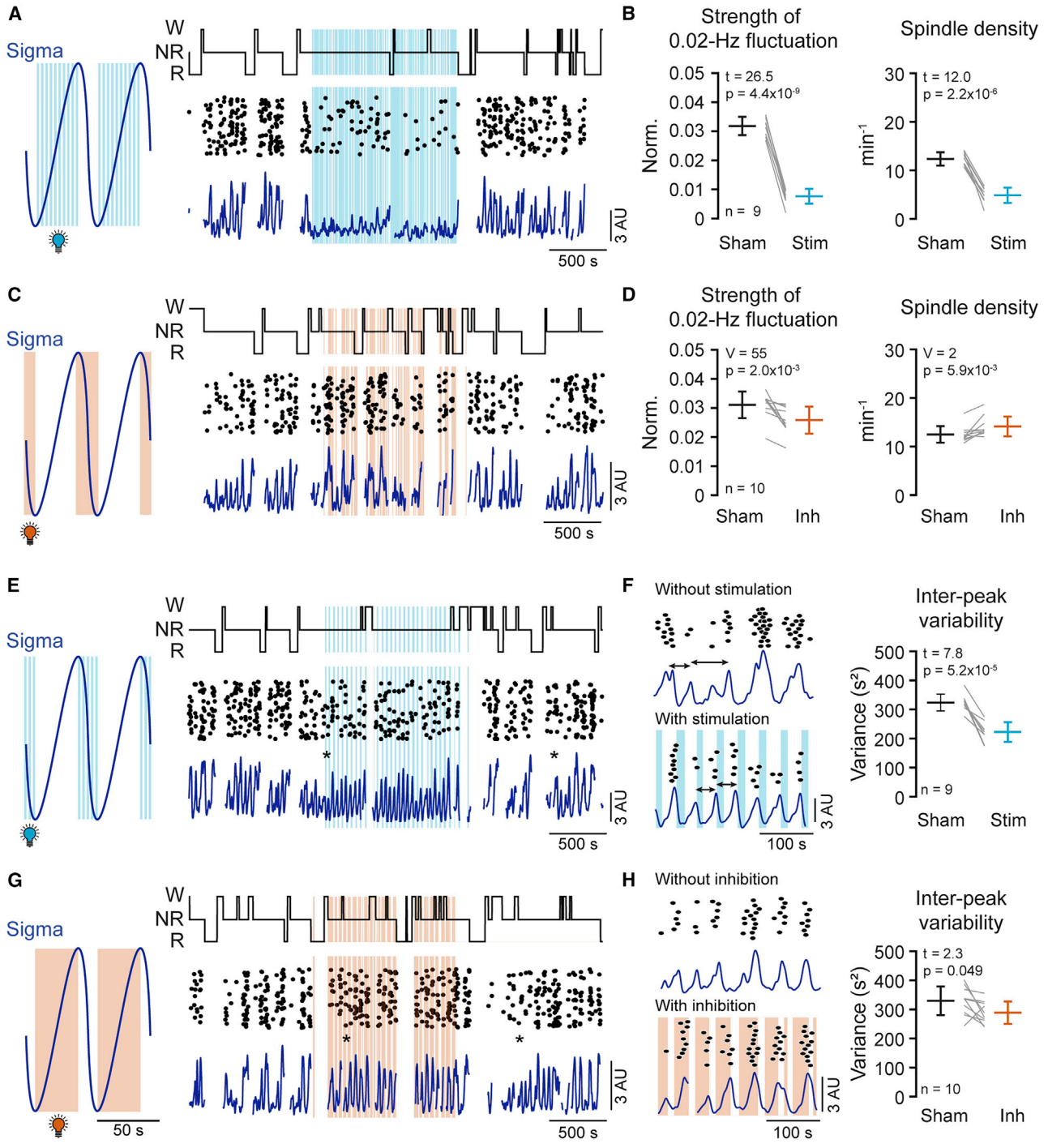

Figure 4. Optogenetic interrogation of LC during spindle-rich or poor periods of NREMS

(A) 1-Hz optogenetic stimulation of LC, restricted to NREMS periods with increasing sigma power. Blue waveform, schematic fluctuation to indicate the timing of the light stimuli. Representative traces are arranged as in Figure 2E.

(B) Quantification of effects on 0.02-Hz fluctuation strength and on spindle density, presented as in Figure 2F.

(C and D) Optogenetic inhibition of LC, restricted to NREMS periods with declining sigma power. Figure panels are analogous to (A) and (B). See also Figures S3 and S4.

(E) Optogenetic stimulation of LC when sigma power declined. Figure panels are analogous to (A) and (C).

(F) Expanded traces, from (*) in (E). Double-headed arrows denote interpeak intervals of the sigma power fluctuation. The regularization of the interpeak intervals in stimulation conditions is quantified through the variance (shown on the right). Note also the tighter temporal alignment between sleep spindles and sigma power. Gray lines show individual animals; black and blue lines show means ± standard error.

(G and H) Optogenetic inhibition of LC when sigma power increased. Figure panels are analogous to (E) and (F).

Please cite this article in press as: Osorio-Forero et al., Noradrenergic circuit control of non-REM sleep substates, Current Biology (2021), https://doi.org/10.1016/j.cub.2021.09.041

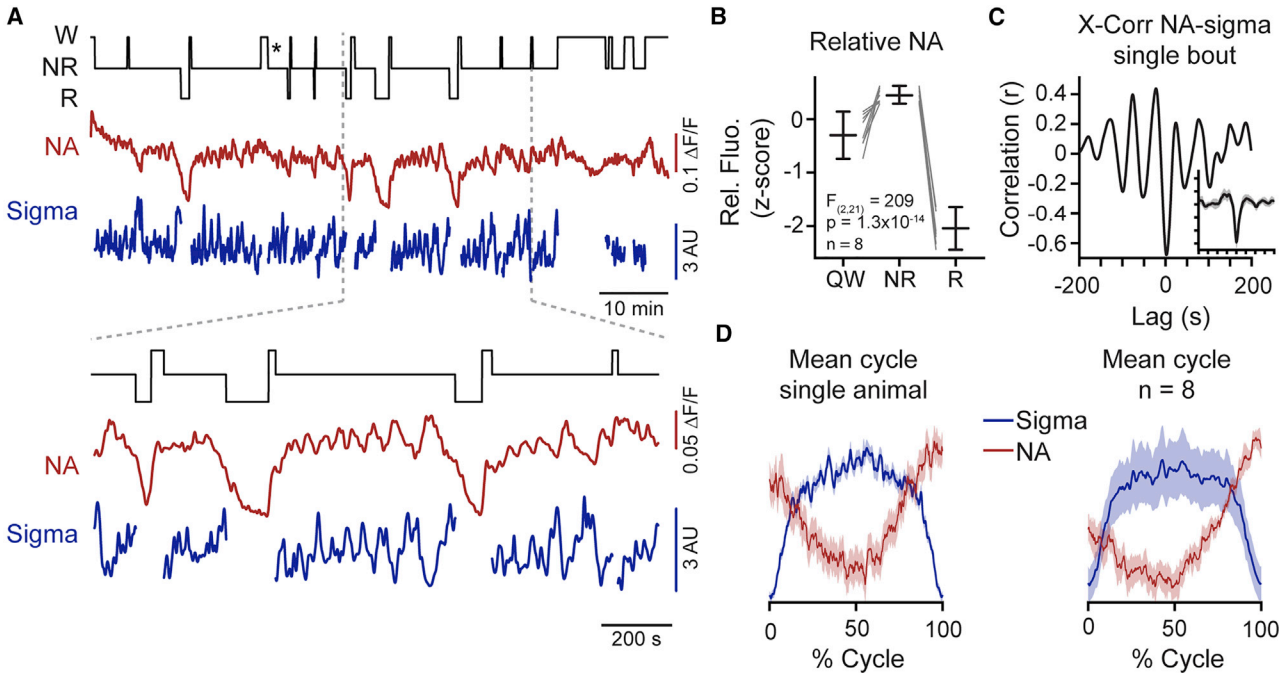

Figure 5. Free noradrenaline levels in thalamus are high and fluctuate during NREMS

(A) Representative recording showing (from top to bottom) hypnogram, relative fluorescence derived from the NA biosensor $GRAB_{NE1h}$, and sigma power dynamics. Expanded portion is shown below. *, bout selected for analysis in (C). See also Figures S5 and S6.

(B) *Z*-scored relative fluorescence derived from the NA biosensor $GRAB_{NE1h}$ in quiet wakefulness (QW), NR, and R. One-way ANOVA followed by post hoc t tests is shown, which yielded: QW versus NR: $t = -4.56$, $p = 2.6 \times 10^{-3}$; QW versus R: $t = 9.27$, $p = 3.35 \times 10^{-5}$; and NR versus R: $t = 39.26$, $p = 1.81 \times 10^{-9}$. Gray lines show individual animals; black lines show means ± standard error.

(C) Cross-correlation (X-Corr) between sigma power and the NA biosensor signal for a single NREMS bout. Inset: means ± standard error for X-Corr across all bouts in the recording, with identical axis scaling.

(D) Left: overlay of mean ± standard error for sigma power dynamics across all infraslow cycles with corresponding NA biosensor signal for one mouse. Right: mean ± standard error across 8 animals.

thalamocortical and thalamic reticular neurons, both of which are involved in sleep-spindle generation.[30] From DBH-Cre mice expressing ChR2 in LC, we prepared coronal thalamic slices and recorded from cells in the ventrobasal complex, which contains the somatosensory thalamus. Thalamocortical and thalamic reticular neurons were distinguished based on location within the slice, membrane potential, and action potential discharge patterns (Figure S7). Optogenetic stimulation induced a slow membrane depolarization for stimulation frequencies at 1, 3, and 10 Hz (Figure 6A). Amplitudes of evoked potentials ranged between 0.8 and 4.5 mV with onset latencies of 1.25–6.9 s and decayed with a slow time course lasting 66–106 s (Figures 6B and S7). Only onset latency was modulated by stimulation frequency. The optogenetically evoked noradrenergic currents measured in cells voltage clamped at −70 mV were blocked by atenolol (10 μM in bath), indicating involvement of β-adrenergic receptors (Figures 6C and 6D).[41] Furthermore, the current response was eliminated by bath application of 1.5–3 mM Cs^+ (Figures 6E and 6F), a blocker of hyperpolarization-activated cation channels.[42] Both atenolol and Cs^+ produced outward currents, indicating a standing receptor and current activation.

To estimate the time course of action of NA on spindle-related cellular activity, we combined optogenetic stimulation of LC fibers with negative current injections to generate repetitive low-threshold burst discharges,[43] known to occur during sleep spindles (Figure 6G).[30] This resulted in a persistent afterdepolarization that was larger and longer than the one generated by cellular bursting alone (Figure 6H). The coincidence of sleep spindle activity with NA release thus generates a prolonged period of cellular depolarization, known to be sufficient to render thalamocortical cells refractory to synaptically driven burst discharge that is necessary to engage in a next sleep spindle.[30,43]

Light-induced depolarizations were also observed in thalamic reticular cells recorded in the somatosensory sector of thalamic reticular nucleus (TRN) (Figures 6I and 6J). Corresponding currents were largely blocked by the α1-adrenergic antagonist prazosin (5 μM in bath; Figures 6K and 6L).[41] However, <15% of TRN cells showed a detectable current response (Figure 6M), suggesting that TRN cells could be heterogeneous in terms of noradrenergic responsiveness. Thalamic reticular cells thus also respond with slowly decaying membrane depolarizations when exposed to NA release from LC fibers.

The LC coordinates heart-rate variations with infraslow brain rhythms

During mouse NREMS, the heart rate (HR) fluctuates on an infraslow timescale and is anticorrelated to sigma power.[27] We conjointly monitored HR and sigma power in freely sleeping C57BL/6J mice (Figures 7A and 7B) and used peripheral cardiac pharmacology to determine which branch of the autonomic

Please cite this article in press as: Osorio-Forero et al., Noradrenergic circuit control of non-REM sleep substates, Current Biology (2021), https://doi.org/10.1016/j.cub.2021.09.041

CellPress
OPEN ACCESS

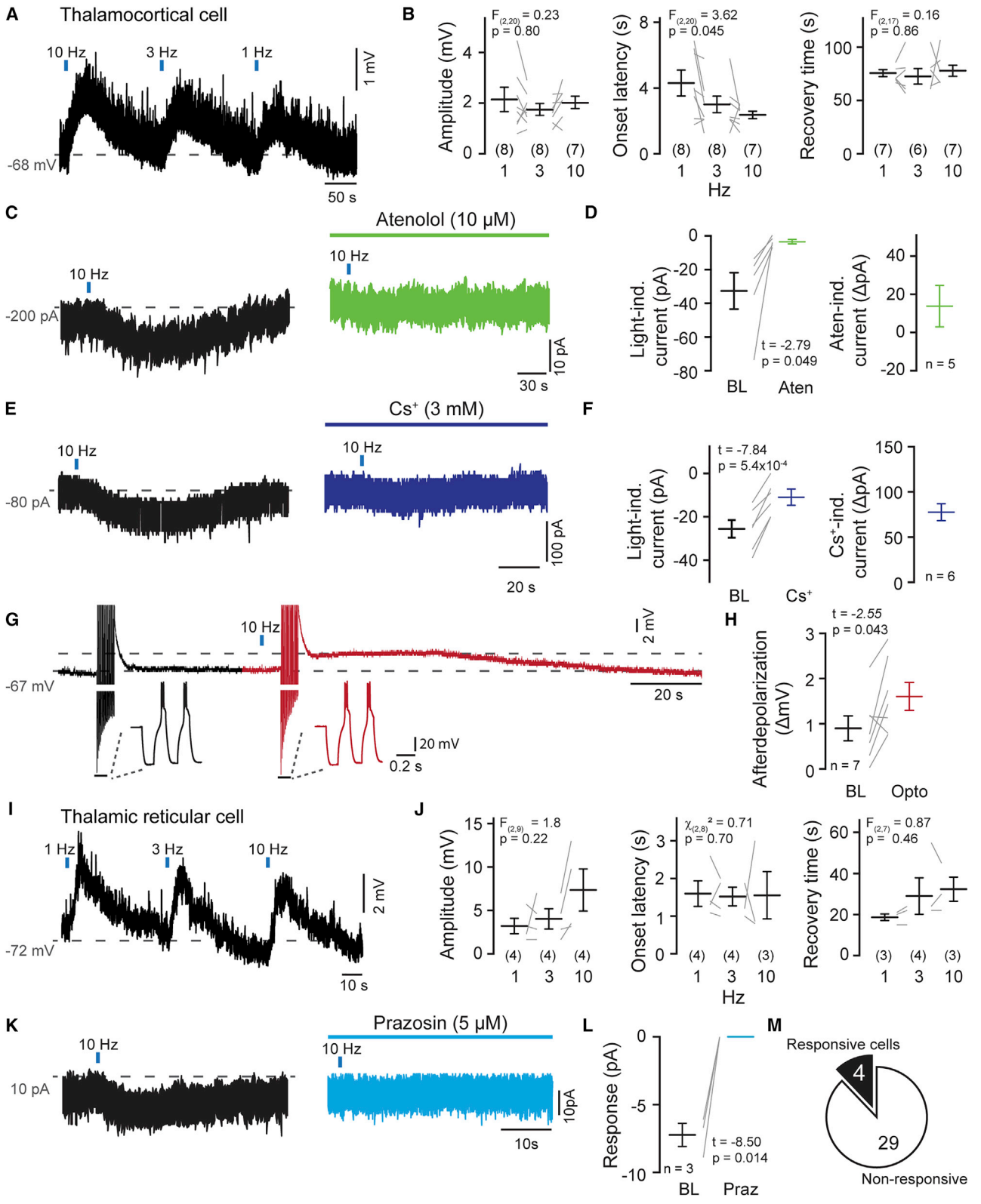

(legend on next page)

Please cite this article in press as: Osorio-Forero et al., Noradrenergic circuit control of non-REM sleep substates, Current Biology (2021), https://doi.org/10.1016/j.cub.2021.09.041

nervous system controlled the infraslow variations in HR. The HR variations were suppressed by the peripheral parasympathetic antagonist methylatropine (10 mg kg^{-1}; Figures 7C and 7D),[44] but not by the peripheral sympathetic antagonist atenolol (1 mg kg^{-1}; Figures 7E and 7F).[45]

LC activity has been implied in parasympathetically driven HR variability in humans[46] and, in rodents, augments inhibitory input to preganglionic cardiac vagal neurons.[47] Therefore, we next tested whether optogenetic manipulation of LC affected variations in HR. Indeed, 1-Hz-LC stimulation during NREMS disrupted the infraslow HR variations (Figure 7G) and decreased their anticorrelation with sigma power (Figure 7H). To directly evaluate the capability of LC in entraining HR variations, we stimulated LC specifically when sigma power declined, as done before (see Figure 4E). This visibly augmented HR variations and imposed anticorrelations with sigma power with side peaks showing an infraslow periodicity (Figures 7I and 7J). These data show that the LC is a source of HR variability during NREMS on an infraslow timescale. Moreover, LC is capable of coordinating sigma power and HR in a manner that supports a critical role in the generation of arousability variations during NREMS.

DISCUSSION

Noradrenergic cell groups in the pontine brainstem are conserved across fish, amphibians, reptiles, birds, and mammals[48–50] and play universal roles during wakefulness, attention, and stress.[15,17–19] Here, we find that NA signaling remained high during NREMS, with mean NA levels exceeding the ones of quiet wakefulness in sensory thalamus, a major subcortical area critical for routing sensory information. Moreover, at intervals close to a minute (~50 s), NA levels fluctuated around this mean, dividing NREMS into two substates previously associated with high and low sensory arousability.[27,28,34] Noradrenergic signaling is thus an integral part of mammalian NREMS. This reverses the conventional notion of NREMS as a state of overall low monoaminergic signaling compared to wakefulness.[6,51] Finally, consistent with the original general hypothesis, mammalian NREMS has an innate and high vulnerability to disruption that arises from powerful wake-promoting circuit control of NREMS substates.

Infraslow LC activity during NREMS could be conserved across mammals

The infraslow timescale has been repeatedly observed in diverse dynamic measures of mammalian NREMS[52] and also appears in reptile sleep,[53] suggesting that fluctuating noradrenergic signaling is phylogenetically preserved. Through timed optogenetic interference, we causally link LC activity to central and autonomic correlates of these fluctuations. In human functional imaging studies of deep NREMS (stage N3), the LC and surrounding areas increase activity in intervals of ~20 s.[24] Moreover, fast spindle activity appears clustered over tens of seconds, in particular during light NREMS (stage N2).[27,32,33] These are timescales compatible with infraslow LC activity in human NREMS. Our study could renew efforts to identify the origins of the human-specific cyclic alternating patterns in the EEG. These events occur preferentially at the beginning and end of a NREMS period and lead to higher arousability every 20–40 s.[54] Intriguingly, the integrity of cyclic alternating patterns has been recently linked to the preservation of noradrenergic signaling in the LC and in forebrain.[55] The implication of LC in other electrical and hemodynamic correlates of infraslow fluctuations also remains to be assessed.[52]

Infraslow noradrenergic fluctuations are found in thalamus and cortex during NREMS

The mean discharge rates of LC units during NREMS presented in pioneering studies from rodent[8–10,20,21,23], cat,[7,11,56] and monkey[8,9] are minor compared to wakefulness. However, subgroups of units showed activity levels remarkably similar for NREMS and quiet wakefulness.[21,23,36] Moreover, some LC units tended to fire in bursts during NREMS,[20] which could increase the amount of NA released.[57,58] Together, LC unit data from NREMS are scarce but seem compatible with the high free NA levels we monitored. Interestingly, free NA levels measured with the GRAB biosensors in mouse prefrontal cortex also overlap for NREMS and wakefulness. These authors overall found higher mean wake NA levels, consistent with strongly variable NA levels across substates of wakefulness and recording conditions.[22] We focused on the early resting phase, when awake animals mostly sit undisturbed and poorly stimulated in their familiar environment. LC activity thus likely remained low in these moments, yet it is possible

Figure 6. Optogenetic LC fiber stimulation *in vitro* evoked slow noradrenergic membrane depolarizations in thalamic neurons

(A) Representative recording from a whole-cell-patched thalamocortical cell exposed to three successive light stimuli (blue bars).

(B) Quantification of evoked response amplitudes, onset latencies, and recovery times as explained in Figure S7. One-way ANOVA followed by post hoc t tests yielded 1 Hz versus 3 Hz: $t = 1.6$, $p = 0.13$; 1 Hz versus 10 Hz: $t = 2.7$, $p = 0.024$; and 3 Hz versus 10 Hz: $t = 1.1$, $p = 0.29$. In this and all panels, gray lines denote results from individual cells; black and colored lines show means ± standard error. See also Figure S7.

(C) Current response in a voltage-clamped thalamocortical neuron, held at −70 mV to 10 Hz light pulses before (left) and after (right) bath application of the β-adrenergic antagonist atenolol.

(D) Left: quantification of light-induced currents in baseline (BL) and Aten. Right: Aten-induced positive holding current shift.

(E and F) Same as (C) and (D) after bath application of Cs^{+}.

(G) Example recording from a thalamocortical neuron injected with repetitive negative current pulses to evoke low-threshold Ca^{2+} bursts, with hyperpolarizing voltage responses and action potentials truncated. Responses to two current pulses are expanded and untruncated in insets. Bursts were followed by an afterdepolarization that was prolonged when light pulses (10 Hz, 4 pulses, blue bar) preceded current injections. Dashed lines aligned to baseline membrane potential and peak of the afterdepolarization.

(H) Quantification of afterdepolarizations in BL (without light exposure) and with light exposure (Opto).

(I and J) As (A) and (B) for a representative recording from a thalamic reticular neuron.

(K) Current response in a voltage-clamped thalamic reticular neuron, held at −70 mV to 10 Hz light pulses before (left) and after (right) bath application of the α1-adrenergic antagonist prazosin.

(L) Quantification of current response amplitude in BL and during Praz.

(M) Number of thalamic reticular neurons responding to LC optogenetic fiber stimulation.

Please cite this article in press as: Osorio-Forero et al., Noradrenergic circuit control of non-REM sleep substates, Current Biology (2021), https://doi.org/10.1016/j.cub.2021.09.041

CellPress
OPEN ACCESS

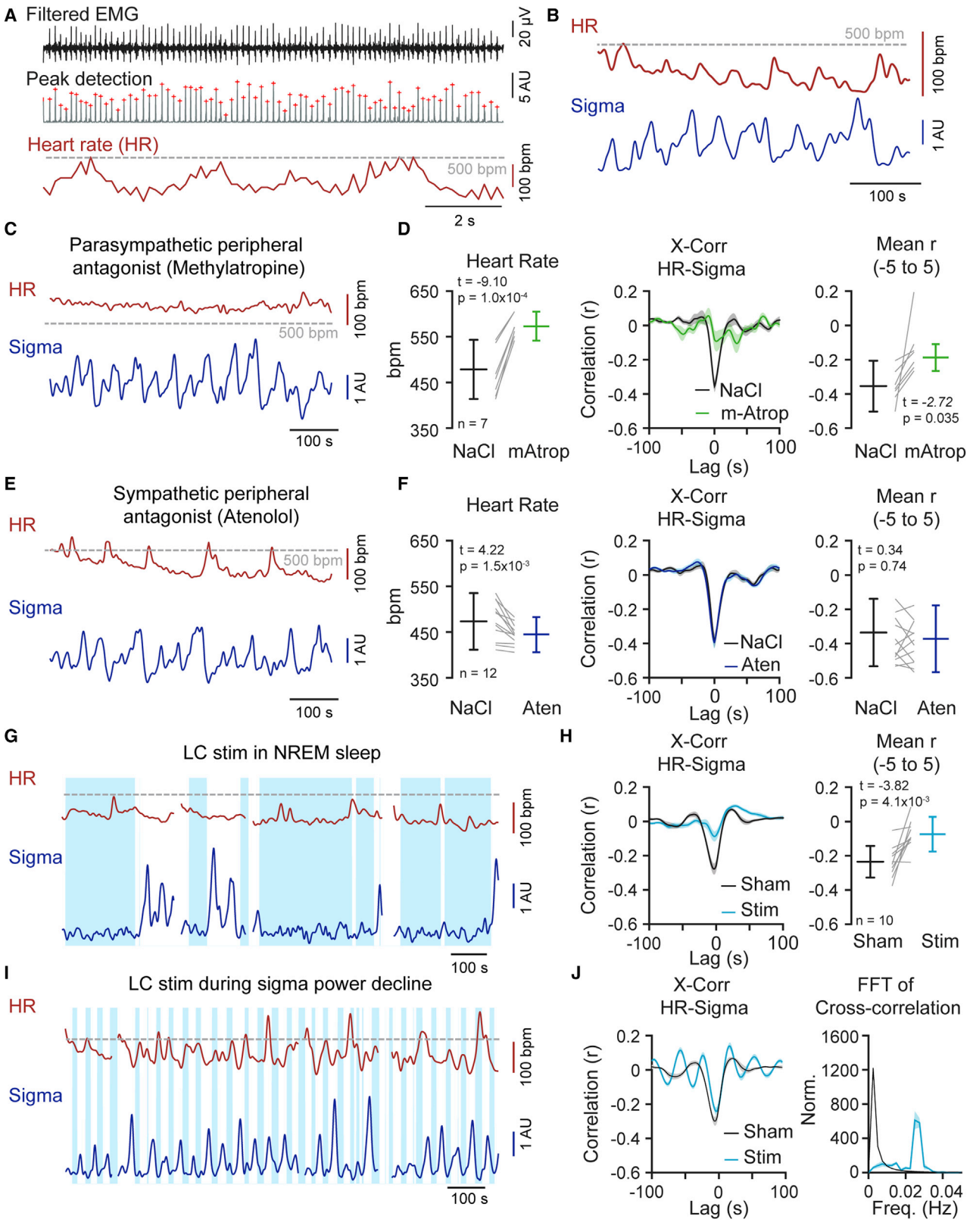

(legend on next page)

Please cite this article in press as: Osorio-Forero et al., Noradrenergic circuit control of non-REM sleep substates, Current Biology (2021), https://doi.org/10.1016/j.cub.2021.09.041

that the NA profile could evolve differently during the dark active, and more attentive, phase of the light-dark cycle, as well as across brain regions.

Measures of intracellular Ca^{2+} levels at the mouse LC cell population level were recently found to peak about once a minute during NREMS,[22] suggesting that numerous LC units are synchronously active on an infraslow timescale. These results combined with ours in sensory thalamus indicate that a fluctuating neuromodulatory tone of NA is an integral part of major thalamocortical circuits during NREMS. Further work is needed to determine the extent to which NA fluctuations generalize across functionally different thalamocortical circuits, as well as to other forebrain areas innervated by LC.

Besides LC, other neuromodulatory systems are known to be active during NREMS. An interesting case is the coincidence of noradrenergic and cholinergic activity that occurs for tens of seconds prior to NREM-REMS transitions[6,12,13] and that gives rise to brief moments of high spindle activity, while hippocampus starts to generate REMS-related theta rhythmicity.[59] Infraslow activity variations during NREMS were recently also reported in REMS-regulating midbrain and medullar neurons[60,61] that target the serotonin-releasing raphe nuclei.[62] Therefore, not only NA but also levels of other neuromodulatory neurotransmitters, such as serotonin, are likely to fluctuate during NREMS.[63]

LC-dependent control of sensory arousability during NREMS

LC activity is known to control sensory arousability through several mechanisms.[17,18] First, LC responds to sensory stimuli;[64] therefore, if LC neurons depolarize and discharge more action potentials, sensory throughput will be facilitated.[16,23] Second, sleep-spindle-related oscillatory electrical activity along the thalamocortical axis protects sleep from external perturbations.[30] These protective effects will be lost when LC activates. Third, sensory-evoked discharge of single or multiple thalamic and cortical units is strengthened by LC stimulation, with thalamic neurons increasing sensory responsiveness more robustly.[18,65] The density of LC fiber varicosities is higher in somatosensory thalamus compared to cortical areas in rat,[39] and DBH immunoreactivity is overall highest in sensorimotor over other cortical areas in human.[66] These findings offer several entry points to further examine how noradrenergic modulation of thalamic circuits facilitates the processing of sensory stimuli during states of NREMS.

Noradrenergic signaling does not terminate spindles but regulates their clustering

Based on sleep spindles measured in EEG[10] and in hippocampal LFPs,[21] the LC is thought to terminate sleep spindles. We establish here a mechanistic opposition between NA levels and spindle-generating circuit activity and can refine this widespread interpretation. Although we suppressed local sleep spindles in S1 via optogenetic LC activation, we could not observe major alterations in sleep-spindle properties when we pharmacologically antagonized noradrenergic signaling in thalamus. Yet in previous work, our spindle-detection algorithm reliably discriminated between fine cortical area-specific sleep-spindle properties.[29] Furthermore, synaptic evoked potentials caused by NA release rose slowly over seconds and are thus unlikely to shortcut individual spindle events. Based on these combined cellular and *in vivo* data, we propose that noradrenergic signaling is tailored to generate prolonged relatively spindle-free periods through depolarizing thalamic neurons, but it does not act rapidly enough to terminate individual spindles.

The cellular and ionic mechanisms underlying noradrenergic control of sleep-spindle clustering

Although infraslow cellular and glial mechanisms have been reported,[43,67] their roles in sleep are open. Through combining *in vivo* and *in vitro* approaches, we identify an infraslow time course of action for NA released from LC terminals that likely underlies sleep-spindle variations. NA induces a slowly decaying membrane depolarization through activation of both $\alpha 1$ or β receptors in thalamocortical and thalamic reticular neurons, which retards the re-engagement of these cells in sleep-spindle generation. Furthermore, we could entrain rhythmically the infraslow fluctuations when we reinforced or attenuated LC activity at appropriate moments. The reinforcement of LC activity most likely triggered membrane depolarizations more consequentially across large cell populations. Conversely, the attenuation of LC activity likely removed spurious LC activity and allowed a more synchronous entry and exit of thalamic circuits within the infraslow cycles. While LC activity thus regulates spindle clustering at the population level, other processes could preferentially terminate spindle activity in individual cells (reviewed in Fernandez and Lüthi[30]). Furthermore, we cannot exclude that the optogenetic interference with LC activity modified cortical and/or brainstem feedback afferents onto LC that could have accelerated its infraslow activity.

The slow membrane depolarizations elicited by low-frequency LC stimulation in the thalamus add to growing evidence that even minor levels of LC activity are functionally efficient in the forebrain.[68,69] Thalamic LC-fiber-elicited responses were present and relatively uniform in amplitude and time course over the 1–10 Hz frequency range. The stability of the response across stimulation frequencies ensures that thalamic membrane potentials are homogeneously depolarized across many

Figure 7. The LC coordinates heart rate and infraslow brain rhythms

(A) Extraction of heart rate (HR) from EMG traces. Raw high-pass-filtered EMG (top), used for peak detection (middle) and HR (bottom) calculation, are shown.
(B) Representative NREMS traces showing sigma power dynamics and corresponding HR after an intraperitoneal (i.p.) injection of NaCl.
(C) Example traces illustrating the effects of the parasympathetic antagonist methylatropine (mAtrop) (10 mg kg^{-1}) on HR and sigma power dynamics.
(D) Left: quantification of mean HR following NaCl or mAtrop injections; middle: corresponding X-Corr; right: values of the X-Corr between −5 and +5 s. Black and colored lines denote means ± standard error in this and all following panels.
(E and F) As (C) and (D) for injection of a sympathetic peripheral antagonist (Aten; 1 mg kg^{-1}).
(G) Example traces illustrating the effects of LC stimulation (stim) in NREMS on HR and sigma power dynamics. See also Figures S3 and S4.
(H) Corresponding X-Corrs quantified as in (D) and (F).
(I) As (G), for LC stimulation restricted to periods of declining sigma power.
(J) Corresponding X-Corr and its Fourier transform highlight the appearance of an infraslow peak.

Please cite this article in press as: Osorio-Forero et al., Noradrenergic circuit control of non-REM sleep substates, Current Biology (2021), https://doi.org/10.1016/j.cub.2021.09.041

CellPress
OPEN ACCESS

neurons. Ultrastructural studies indeed suggest that noradrenergic terminals in the rodent ventrobasal thalamic complex do not form well-defined synaptic contacts,[70] suggesting that released NA may diffuse from the site of release into the extracellular medium. In support of such a signaling scheme, we find that noradrenergic receptors activated by optogenetic LC fiber stimulation are the same as the ones targeted by bath-applied NA.[41]

Noradrenergic signaling is a source of HR variations during NREMS

We identified the parasympathetic system to underlie the infraslow variations in HR, as was also observed for infraslow pupil diameter variations.[34] The LC increases HR through several pathways, in part through a suppression of activity in the parasympathetic preganglionic vagal nuclei.[47] Our data suggest that this pathway could play a role in HR regulation during NREMS. Furthermore, 1-Hz stimulation during NREMS abolished infraslow HR variations, demonstrating that LC coordinates the infraslow activity patterns in brain and heart. Such coordinated fluctuations suggest that LC units become synchronized across dorsal and ventral regions of the LC, in which forebrain- and hindbrain-projecting cells preferentially reside, respectively.[71] Appropriate timing of LC stimulation also increased the fluctuations of the HR and strengthened central and peripheral coordination on the infraslow timescale. The direct demonstration of LC's role in HR variability will renew interest in the varied autonomic and central manifestations of arousal-like events during NREMS.[72]

We find that mammalian sleep harnesses on wake promotion to enable sensory vigilance. This insight requires a renewal of current models of sleep-wake control in which reciprocal and exclusive antagonism is prevalent between sleep- and wake-promoting brain areas, including the LC.[6] Still, the origins of how LC becomes periodically activated and overcomes this antagonism during NREMS remain to be addressed. On the one hand, the LC is engaged in multiple and recurrent input-output loops across fore-, mid-, and hindbrain that could induce infraslow rhythms through the summed actions of slow synaptic inputs.[71] Of particular interest are recent studies identifying infraslow fluctuations of neuronal activity in midbrain and dorsomedullar areas involved in the regulation of NREM-REMS cycle that innervate LC.[60,61] Alternatively, it is important to consider that the majority of LC neurons respond sensitively to CO_2 and pH changes.[73] Such chemosensation may activate LC during NREMS, for example, in response to pulsatile brain fluid exchange that, intriguingly, is anticorrelated to infraslow hemodynamic signals.[74] Based on such mechanistic insights, it will be interesting to probe whether the enhanced appearance of cyclic alternating patterns in cases of sleep-related breathing disorders, such as sleep apnea, can be controlled with noradrenergic antagonists.[54] Furthermore, there is strong evidence that LC and sleep disruptions could be linked in post-traumatic stress disorders;[18] in neurodegenerative diseases, such as Alzheimer's and Parkinson's disease;[75] and in insomnia.[5] We are now able to concretize questions into possible noradrenergic origins of a large variety of primary and secondary sleep disorders, in which hyperarousals, autonomic arousals, and movement-related arousals prominently feature.

STAR★METHODS

Detailed methods are provided in the online version of this paper and include the following:

- KEY RESOURCES TABLE
- RESOURCE AVAILABILITY
  - Lead contact
  - Materials availability
  - Data and code availability
- EXPERIMENTAL MODEL AND SUBJECT DETAILS
  - Subjects
- METHOD DETAILS
  - Viral injections
  - Other surgical procedures
  - *In vivo* electrophysiological recordings
  - Procedures for intracranial pharmacology
  - Procedures for *in vivo* optogenetics
  - Procedures for *in vivo* fiber photometry
  - *In vitro* electrophysiological recordings
  - Pharmacological manipulation of heart rate
  - Histology
- QUANTIFICATION AND STATISTICAL ANALYSIS
  - *In vivo* data analysis
  - Statistical analysis

SUPPLEMENTAL INFORMATION

Supplemental information can be found online at https://doi.org/10.1016/j.cub.2021.09.041.

ACKNOWLEDGMENTS

We thank Paul Steffan and Dr. David McCormick for providing us with the original DBH-Cre breeders. We greatly appreciate the time-efficient support provided to us from Drs. Yulong Li and Jessie Feng regarding the NA sniffers. Particular thanks go to the animal caretaking team headed by Michelle Blom and to Titouan Tromme, who took so good care of our animal lines. Expert veterinary advice was given by Drs. Delphine Perret and Laure Sériot. We thank Dr. Jean Pierre Hornung for support in histological analysis. We appreciate the helpful exchange regarding optogenetic LC manipulation and NA sniffer experimentation with Drs. Simone Astori, Antoine Adamantidis, Ernesto Durán, Oxana Eschenko, Jessie Feng, Paul Franken, Celia Kjaerby, Maiken Nedergaard, Niels Niethard, Patricia Bonnavion, and Andrea Volterra. We are indebted to Francesca Siclari, Christoph Michel, and Francesco Petrelli for insightful discussions on the human noradrenergic system. Simone Astori, Francesca Siclari, and Freddy Weber provided valuable input on preliminary versions of the manuscript. All lab members provided constructive input to this study throughout the experimental period and to preliminary versions of the manuscript. This study was funded by The Swiss National Science Foundation (no. 310030-184759 to A.L.), Etat de Vaud, and a FBM UNIL PhD Fellowship to A.O.-F.

AUTHOR CONTRIBUTIONS

Conceptualization, A.L., A.O.-F., R.C., and L.M.J.F.; methodology, A.L. and A.O.-F.; software, A.O.-F. and R.C.; validation, A.L., A.O.-F., R.C., and L.M.J.F.; formal analysis, A.O.-F.; investigation, A.O.-F., R.C., G.V., A.G.-G., and G.K.; resources, A.L. and A.O.-F.; data curation, A.O.-F. and L.M.J.F.; writing – original draft, A.L. and A.O.-F.; writing – review & editing, L.M.J.F., R.C., G.V., A.G.-G., G.K., A.O.-F., and A.L.; visualization, A.O.-F. and L.M.J.F.; supervision, A.L.; project administration, A.L.; funding acquisition, A.L. and A.O.-F.

Please cite this article in press as: Osorio-Forero et al., Noradrenergic circuit control of non-REM sleep substates, Current Biology (2021), https://doi.org/10.1016/j.cub.2021.09.041

DECLARATION OF INTERESTS

The authors declare no competing interests. A.L. is a member of the journal's advisory board.

Received: May 11, 2021
Revised: August 9, 2021
Accepted: September 15, 2021
Published: October 13, 2021

REFERENCES

1. Van Someren, E.J., Cirelli, C., Dijk, D.J., Van Cauter, E., Schwartz, S., and Chee, M.W. (2015). Disrupted sleep: from molecules to cognition. J. Neurosci. *35*, 13889–13895.
2. Mascetti, G.G. (2021). Adaptation and survival: hypotheses about the neural mechanisms of unihemispheric sleep. Laterality *26*, 71–93.
3. Mander, B.A., Winer, J.R., and Walker, M.P. (2017). Sleep and human aging. Neuron *94*, 19–36.
4. Siclari, F., Valli, K., and Arnulf, I. (2020). Dreams and nightmares in healthy adults and in patients with sleep and neurological disorders. Lancet Neurol. *19*, 849–859.
5. Van Someren, E.J.W. (2021). Brain mechanisms of insomnia: new perspectives on causes and consequences. Physiol. Rev. *101*, 995–1046.
6. Saper, C.B., Fuller, P.M., Pedersen, N.P., Lu, J., and Scammell, T.E. (2010). Sleep state switching. Neuron *68*, 1023–1042.
7. Chu, N.S., and Bloom, F.E. (1974). Activity patterns of catecholamine-containing pontine neurons in the dorso-lateral tegmentum of unrestrained cats. J. Neurobiol. *5*, 527–544.
8. Foote, S.L., Aston-Jones, G., and Bloom, F.E. (1980). Impulse activity of locus coeruleus neurons in awake rats and monkeys is a function of sensory stimulation and arousal. Proc. Natl. Acad. Sci. USA *77*, 3033–3037.
9. Rajkowski, J., Kubiak, P., and Aston-Jones, G. (1994). Locus coeruleus activity in monkey: phasic and tonic changes are associated with altered vigilance. Brain Res. Bull. *35*, 607–616.
10. Aston-Jones, G., and Bloom, F.E. (1981). Activity of norepinephrine-containing locus coeruleus neurons in behaving rats anticipates fluctuations in the sleep-waking cycle. J. Neurosci. *1*, 876–886.
11. Hobson, J.A., McCarley, R.W., and Wyzinski, P.W. (1975). Sleep cycle oscillation: reciprocal discharge by two brainstem neuronal groups. Science *189*, 55–58.
12. el Mansari, M., Sakai, K., and Jouvet, M. (1989). Unitary characteristics of presumptive cholinergic tegmental neurons during the sleep-waking cycle in freely moving cats. Exp. Brain Res. *76*, 519–529.
13. Kayama, Y., Ohta, M., and Jodo, E. (1992). Firing of 'possibly' cholinergic neurons in the rat laterodorsal tegmental nucleus during sleep and wakefulness. Brain Res. *569*, 210–220.
14. Dahlstroem, A., and Fuxe, K. (1964). Evidence for the existence of monoamine-containing neurons in the central nervous system. I. Demonstration of monoamines in the cell bodies of brain stem neurons. Acta Physiol. Scand. Suppl. *232*, 1–55.
15. Berridge, C.W. (2008). Noradrenergic modulation of arousal. Brain Res. Brain Res. Rev. *58*, 1–17.
16. Carter, M.E., Yizhar, O., Chikahisa, S., Nguyen, H., Adamantidis, A., Nishino, S., Deisseroth, K., and de Lecea, L. (2010). Tuning arousal with optogenetic modulation of locus coeruleus neurons. Nat. Neurosci. *13*, 1526–1533.
17. Aston-Jones, G., and Cohen, J.D. (2005). An integrative theory of locus coeruleus-norepinephrine function: adaptive gain and optimal performance. Annu. Rev. Neurosci. *28*, 403–450.
18. Poe, G.R., Foote, S., Eschenko, O., Johansen, J.P., Bouret, S., Aston-Jones, G., Harley, C.W., Manahan-Vaughan, D., Weinshenker, D., Valentino, R., et al. (2020). Locus coeruleus: a new look at the blue spot. Nat. Rev. Neurosci. *21*, 644–659.
19. Sara, S.J., and Bouret, S. (2012). Orienting and reorienting: the locus coeruleus mediates cognition through arousal. Neuron *76*, 130–141.
20. Eschenko, O., Magri, C., Panzeri, S., and Sara, S.J. (2012). Noradrenergic neurons of the locus coeruleus are phase locked to cortical up-down states during sleep. Cereb. Cortex *22*, 426–435.
21. Swift, K.M., Gross, B.A., Frazer, M.A., Bauer, D.S., Clark, K.J.D., Vazey, E.M., Aston-Jones, G., Li, Y., Pickering, A.E., Sara, S.J., and Poe, G.R. (2018). Abnormal locus coeruleus sleep activity alters sleep signatures of memory consolidation and impairs place cell stability and spatial memory. Curr. Biol. *28*, 3599–3609.e4.
22. Kjaerby, C., Andersen, M., Hauglund, N., Ding, F., Wang, W., Xu, Q., Deng, S., Kang, N., Peng, S., Sun, Q., et al. (2020). Dynamic fluctuations of the locus coeruleus-norepinephrine system underlie sleep state transitions. bioRxiv. https://doi.org/10.1101/2020.09.01.274977.
23. Hayat, H., Regev, N., Matosevich, N., Sales, A., Paredes-Rodriguez, E., Krom, A.J., Bergman, L., Li, Y., Lavigne, M., Kremer, E.J., et al. (2020). Locus coeruleus norepinephrine activity mediates sensory-evoked awakenings from sleep. Sci. Adv. *6*, eaaz4232.
24. Dang-Vu, T.T., Schabus, M., Desseilles, M., Albouy, G., Boly, M., Darsaud, A., Gais, S., Rauchs, G., Sterpenich, V., Vandewalle, G., et al. (2008). Spontaneous neural activity during human slow wave sleep. Proc. Natl. Acad. Sci. USA *105*, 15160–15165.
25. Gais, S., Rasch, B., Dahmen, J.C., Sara, S., and Born, J. (2011). The memory function of noradrenergic activity in non-REM sleep. J. Cogn. Neurosci. *23*, 2582–2592.
26. Zerbi, V., Floriou-Servou, A., Markicevic, M., Vermeiren, Y., Sturman, O., Privitera, M., von Ziegler, L., Ferrari, K.D., Weber, B., De Deyn, P.P., et al. (2019). Rapid reconfiguration of the functional connectome after chemogenetic *locus coeruleus* activation. Neuron *103*, 702–718.e5.
27. Lecci, S., Fernandez, L.M.J., Weber, F.D., Cardis, R., Chatton, J.-Y., Born, J., and Lüthi, A. (2017). Coordinated infraslow neural and cardiac oscillations mark fragility and offline periods in mammalian sleep. Sci. Adv. *3*, e1602026.
28. Cardis, R., Lecci, S., Fernandez, L.M., Osorio-Forero, A., Chu Sin Chung, P., Fulda, S., Decosterd, I., and Lüthi, A. (2021). Cortico-autonomic local arousals and heightened somatosensory arousability during NREMS of mice in neuropathic pain. eLife *10*, e65835.
29. Fernandez, L.M., Vantomme, G., Osorio-Forero, A., Cardis, R., Béard, E., and Lüthi, A. (2018). Thalamic reticular control of local sleep in mouse sensory cortex. eLife *7*, e39111.
30. Fernandez, L.M.J., and Lüthi, A. (2020). Sleep spindles: mechanisms and functions. Physiol. Rev. *100*, 805–868.
31. Andrillon, T., and Kouider, S. (2020). The vigilant sleeper: neural mechanisms of sensory (de)coupling during sleep. Curr. Opin. Physiol. *15*, 47–59.
32. Lázár, Z.I., Dijk, D.J., and Lázár, A.S. (2019). Infraslow oscillations in human sleep spindle activity. J. Neurosci. Methods *316*, 22–34.
33. Antony, J.W., Piloto, L., Wang, M., Pacheco, P., Norman, K.A., and Paller, K.A. (2018). Sleep spindle refractoriness segregates periods of memory reactivation. Curr. Biol. *28*, 1736–1743.e4.
34. Yüzgeç, Ö., Prsa, M., Zimmermann, R., and Huber, D. (2018). Pupil size coupling to cortical states protects the stability of deep sleep via parasympathetic modulation. Curr. Biol. *28*, 392–400.e3.
35. Harris, J.A., Hirokawa, K.E., Sorensen, S.A., Gu, H., Mills, M., Ng, L.L., Bohn, P., Mortrud, M., Ouellette, B., Kidney, J., et al. (2014). Anatomical characterization of Cre driver mice for neural circuit mapping and manipulation. Front. Neural Circuits *8*, 76.
36. Eschenko, O., and Sara, S.J. (2008). Learning-dependent, transient increase of activity in noradrenergic neurons of locus coeruleus during slow wave sleep in the rat: brain stem-cortex interplay for memory consolidation? Cereb. Cortex *18*, 2596–2603.
37. Stujenske, J.M., Spellman, T., and Gordon, J.A. (2015). Modeling the spatiotemporal dynamics of light and heat propagation for in vivo optogenetics. Cell Rep. *12*, 525–534.

Please cite this article in press as: Osorio-Forero et al., Noradrenergic circuit control of non-REM sleep substates, Current Biology (2021), https://doi.org/10.1016/j.cub.2021.09.041

38. Wyatt, R.J., Chase, T.N., Kupfer, D.J., Scott, J., and Snyder, F. (1971). Brain catecholamines and human sleep. Nature *233*, 63–65.

39. Agster, K.L., Mejias-Aponte, C.A., Clark, B.D., and Waterhouse, B.D. (2013). Evidence for a regional specificity in the density and distribution of noradrenergic varicosities in rat cortex. J. Comp. Neurol. *521*, 2195–2207.

40. Feng, J., Zhang, C., Lischinsky, J.E., Jing, M., Zhou, J., Wang, H., Zhang, Y., Dong, A., Wu, Z., Wu, H., et al. (2019). A genetically encoded fluorescent sensor for rapid and specific *in vivo* detection of norepinephrine. Neuron *102*, 745–761.e8.

41. Lee, K.H., and McCormick, D.A. (1996). Abolition of spindle oscillations by serotonin and norepinephrine in the ferret lateral geniculate and perigeniculate nuclei *in vitro*. Neuron *17*, 309–321.

42. Lüthi, A., and McCormick, D.A. (1998). H-current: properties of a neuronal and network pacemaker. Neuron *21*, 9–12.

43. Lüthi, A., and McCormick, D.A. (1998). Periodicity of thalamic synchronized oscillations: the role of Ca^{2+}-mediated upregulation of I_h. Neuron *20*, 553–563.

44. Smith, R.D., Grzelak, M.E., and Coffin, V.L. (1994). Methylatropine blocks the central effects of cholinergic antagonists. Behav. Pharmacol. *5*, 167–175.

45. Neil-Dwyer, G., Bartlett, J., McAinsh, J., and Cruickshank, J.M. (1981). β-adrenoceptor blockers and the blood-brian barrier. Br. J. Clin. Pharmacol. *11*, 549–553.

46. Mather, M., Joo Yoo, H., Clewett, D.V., Lee, T.H., Greening, S.G., Ponzio, A., Min, J., and Thayer, J.F. (2017). Higher locus coeruleus MRI contrast is associated with lower parasympathetic influence over heart rate variability. Neuroimage *150*, 329–335.

47. Wang, X., Piñol, R.A., Byrne, P., and Mendelowitz, D. (2014). Optogenetic stimulation of locus ceruleus neurons augments inhibitory transmission to parasympathetic cardiac vagal neurons via activation of brainstem α1 and β1 receptors. J. Neurosci. *34*, 6182–6189.

48. Noronha-de-Souza, C.R., Bícego, K.C., Michel, G., Glass, M.L., Branco, L.G., and Gargaglioni, L.H. (2006). Locus coeruleus is a central chemoreceptive site in toads. Am. J. Physiol. Regul. Integr. Comp. Physiol. *291*, R997–R1006.

49. Smeets, W.J., and González, A. (2000). Catecholamine systems in the brain of vertebrates: new perspectives through a comparative approach. Brain Res. Brain Res. Rev. *33*, 308–379.

50. Totah, N.K.B., Logothetis, N.K., and Eschenko, O. (2019). Noradrenergic ensemble-based modulation of cognition over multiple timescales. Brain Res. *1709*, 50–66.

51. Jones, B.E. (2020). Arousal and sleep circuits. Neuropsychopharmacology *45*, 6–20.

52. Watson, B.O. (2018). Cognitive and physiologic impacts of the infraslow oscillation. Front. Syst. Neurosci. *12*, 44.

53. Libourel, P.A., Barrillot, B., Arthaud, S., Massot, B., Morel, A.L., Beuf, O., Herrel, A., and Luppi, P.H. (2018). Partial homologies between sleep states in lizards, mammals, and birds suggest a complex evolution of sleep states in amniotes. PLoS Biol. *16*, e2005982.

54. Parrino, L., Ferri, R., Bruni, O., and Terzano, M.G. (2012). Cyclic alternating pattern (CAP): the marker of sleep instability. Sleep Med. Rev. *16*, 27–45.

55. Doppler, C.E.J., Smit, J.A.M., Hommelsen, M., Seger, A., Horsager, J., Kinnerup, M.B., Hansen, A.K., Fedorova, T.D., Knudsen, K., Otto, M., et al. (2021). Microsleep disturbances are associated with noradrenergic dysfunction in Parkinson's disease. Sleep *44*, zsab040.

56. Rasmussen, K., Morilak, D.A., and Jacobs, B.L. (1986). Single unit activity of locus coeruleus neurons in the freely moving cat. I. During naturalistic behaviors and in response to simple and complex stimuli. Brain Res. *371*, 324–334.

57. Florin-Lechner, S.M., Druhan, J.P., Aston-Jones, G., and Valentino, R.J. (1996). Enhanced norepinephrine release in prefrontal cortex with burst stimulation of the locus coeruleus. Brain Res. *742*, 89–97.

58. Dugast, C., Cespuglio, R., and Suaud-Chagny, M.F. (2002). In vivo monitoring of evoked noradrenaline release in the rat anteroventral thalamic nucleus by continuous amperometry. J. Neurochem. *82*, 529–537.

59. Durán, E., Oyanedel, C.N., Niethard, N., Inostroza, M., and Born, J. (2018). Sleep stage dynamics in neocortex and hippocampus. Sleep (Basel) *41*, zsy060.

60. Stucynski, J.A., Schott, A.L., Baik, J., Chung, S., and Weber, F. (2021). Regulation of REM sleep by inhibitory neurons in the dorsomedial medulla. bioRxiv. https://doi.org/10.1101/2020.11.30.405530.

61. Weber, F., Hoang Do, J.P., Chung, S., Beier, K.T., Bikov, M., Saffari Doost, M., and Dan, Y. (2018). Regulation of REM and non-REM sleep by periaqueductal GABAergic neurons. Nat. Commun. *9*, 354.

62. Gervasoni, D., Peyron, C., Rampon, C., Barbagli, B., Chouvet, G., Urbain, N., Fort, P., and Luppi, P.H. (2000). Role and origin of the GABAergic innervation of dorsal raphe serotonergic neurons. J. Neurosci. *20*, 4217–4225.

63. Wan, J., Peng, W., Li, X., Qian, T., Song, K., Zheng, J., et al. (2021). A genetically encoded sensor for measuring serotonin dynamics. Nat. Neurosci. *24*, 746–752.

64. Takahashi, K., Kayama, Y., Lin, J.S., and Sakai, K. (2010). Locus coeruleus neuronal activity during the sleep-waking cycle in mice. Neuroscience *169*, 1115–1126.

65. Devilbiss, D.M., and Waterhouse, B.D. (2004). The effects of tonic locus ceruleus output on sensory-evoked responses of ventral posterior medial thalamic and barrel field cortical neurons in the awake rat. J. Neurosci. *24*, 10773–10785.

66. Gaspar, P., Berger, B., Febvret, A., Vigny, A., and Henry, J.P. (1989). Catecholamine innervation of the human cerebral cortex as revealed by comparative immunohistochemistry of tyrosine hydroxylase and dopamine-beta-hydroxylase. J. Comp. Neurol. *279*, 249–271.

67. Hughes, S.W., Lörincz, M.L., Parri, H.R., and Crunelli, V. (2011). Infraslow (<0.1 Hz) oscillations in thalamic relay nuclei basic mechanisms and significance to health and disease states. Prog. Brain Res. *193*, 145–162.

68. Bacon, T.J., Pickering, A.E., and Mellor, J.R. (2020). Noradrenaline release from locus coeruleus terminals in the hippocampus enhances excitation-spike coupling in CA1 pyramidal neurons via β-adrenoceptors. Cereb. Cortex *30*, 6135–6151.

69. Liang, Y., Shi, W., Xiang, A., Hu, D., Wang, L., and Zhang, L. (2021). The NAergic locus coeruleus-ventrolateral preoptic area neural circuit mediates rapid arousal from sleep. Curr. Biol. *31*, 3729–3742.e5.

70. Nothias, F., Onteniente, B., Roudier, F., and Peschanksi, M. (1988). Immunocytochemical study of serotoninergic and noradrenergic innervation of the ventrobasal complex of the rat thalamus. Neurosci. Lett. *95*, 59–63.

71. Schwarz, L.A., and Luo, L. (2015). Organization of the locus coeruleus-norepinephrine system. Curr. Biol. *25*, R1051–R1056.

72. Parrino, L., Halasz, P., Tassinari, C.A., and Terzano, M.G. (2006). CAP, epilepsy and motor events during sleep: the unifying role of arousal. Sleep Med. Rev. *10*, 267–285.

73. Madan, V., and Jha, S.K. (2012). A moderate increase of physiological CO(2) in a critical range during stable NREM sleep episode: a potential gateway to REM sleep. Front. Neurol. *3*, 19.

74. Fultz, N.E., Bonmassar, G., Setsompop, K., Stickgold, R.A., Rosen, B.R., Polimeni, J.R., and Lewis, L.D. (2019). Coupled electrophysiological, hemodynamic, and cerebrospinal fluid oscillations in human sleep. Science *366*, 628–631.

75. Kelberman, M., Keilholz, S., and Weinshenker, D. (2020). What's that (blue) spot on my MRI? Multimodal neuroimaging of the locus coeruleus in neurodegenerative disease. Front. Neurosci. *14*, 583421.

76. Vantomme, G., Rovó, Z., Cardis, R., Béard, E., Katsioudi, G., Guadagno, A., Perrenoud, V., Fernandez, L.M.J., and Lüthi, A. (2020). A thalamic reticular circuit for head direction cell tuning and spatial navigation. Cell Rep. *31*, 107747.

Please cite this article in press as: Osorio-Forero et al., Noradrenergic circuit control of non-REM sleep substates, Current Biology (2021), https://doi.org/10.1016/j.cub.2021.09.041

STAR★METHODS

KEY RESOURCES TABLE

REAGENT or RESOURCE	SOURCE	IDENTIFIER
Antibodies		
Goat anti-mouse Alexa Fluor 488	Invitrogen	Cat# A32723; RRID: AB_2633275
Mouse anti-TH	Immunostar	Cat# 22941; RRID:AB_572268
Rabbit polyclonal Anti-mCherry	abcam	Cat# Ab183628; RRID:AB_2650480
Donkey anti-Rabbit Alexa Fluo 594	Invitrogen	Cat# R37119; RRID: AB_2556547
Bacterial and virus strains		
ssAAV5/2-hEF1 α-dlox-hChR2(H134R) mCherry(rev)-dlox-WPRE-hGHp(A)	VVF Zurich	v80-5
pAAV5-CAG-FLEX-rc [Jaws-KGC-GFP-ER2]	Addgene	84445-AAV5
AAV8-hSyn-FLEX-Jaws-KGC-GFP-ER2	UNC Vector Core	N/A
ssAAV-5/2-hSyn1-dlox-Jaws_KGC_EGFP_ERES(rev)-dlox-WPRE-bGHp(A)-SV40p(A)	VVF Zurich	v508-5
ssAAV5/2-hEF1α-dlox-mCherry(rev)-dlox-WPRE-hGHp(A)	VVF Zurich	V218-5
ssAAV9/2-hSyn1-GRAB_NEh-WPRE-hGHp(A)	VVF Zurich	v472-9
ssAAV9/2-hSyn1-GRAB_NEm-WPRE-hGHp(A)	VVF Zurich	v471-9
Chemicals, peptides, and recombinant proteins		
(S)-(-)-atenolol	Sigma-Aldrich	A7655
Prazosin hydrochloride	Sigma-Aldrich	P7791
Methylatropine bromide	Sigma-Aldrich	M1300000
Cesium chloride	Sigma-Aldrich	C3032-25G
Deposited data		
Raw and analyzed data	This paper	https://doi.org/10.5281/zenodo.5520888
MATLAB code	This paper	available from lead contact on request, see also https://github.com/Romain2-5/IntanLuthiLab.
Experimental models: Organisms/strains		
M. musculus, C57BL/6J	Jackson Laboratory	Jax: 000664
M. musculus, B6.FVB(Cg)-Tg(Dbh-cre) KH212Gsat/Mmucd	MMRRC, University of California, Davis	MMRRC_036778-UCD
Software and algorithms		
NIS-Elements 4.5	Nikon	N/A
Zen lite 2012	Zeiss	N/A
Adobe Photoshop 2020	Adobe Creative Cloud	N/A
Adobe Illustrator 2020, 2021	Adobe Creative Cloud	N/A
Clampex10.2	Molecular Devices	N/A
Clampfit v2.2	Molecular Devices	N/A
R 3.5.1	R Core Team	N/A
MATLAB 2015b, 2018a	MathWorks	N/A
Excel	Microsoft	N/A

Please cite this article in press as: Osorio-Forero et al., Noradrenergic circuit control of non-REM sleep substates, Current Biology (2021), https://doi.org/10.1016/j.cub.2021.09.041

CellPress
OPEN ACCESS

RESOURCE AVAILABILITY

Lead contact

For information and request for resources should be directed to the lead contact, Anita Lüthi (anita.luthi@unil.ch)

Materials availability

The study did not produce any new materials or reagents.

Data and code availability

All data included in this publication will be stored on one of the servers of the University of Lausanne and will be made available by the lead contact upon request (https://doi.org/10.5281/zenodo.5520888). All Customized MATLAB scripts for analysis are available from the corresponding author upon reasonable request. For data acquisition and scoring, MATLAB scripts are available in the following GitHub repository: https://github.com/Romain2-5/IntanLuthiLab.

EXPERIMENTAL MODEL AND SUBJECT DETAILS

Subjects

Mice from the C57BL/6J line and from the B6.FVB(Cg)-Tg(Dbh-cre)KH212Gsat/Mmucd (MMRRC Stock#036778-UCD) line,[35] referred to here as DBH-Cre line, were bred on a C57BL/6J background and housed in a humidity- and temperature-controlled animal house with a 12 h / 12 h light-dark cycle (lights on at 9 am). Food and water were available *ad libitum* throughout all the experimental procedures. For viral injections, 2- to 7-week-old mice of either sex were transferred to a P2 safety level housing room with identical conditions 1 d prior to injection. For *in vivo* experimentation, animals were transferred to the recording room 3 d after viral injection and left to recover for at least 1 week prior to the implantation surgery, after which they were singly housed in standard-sized cages. The grids on top of the cage were removed and replaced by 30 cm-high Plexiglass walls. Fresh food was regularly placed on the litter and the water bottle inserted through a hole in the cage wall. Objects (tissues, paper rolls, ping-pong balls) were given for enrichment. For *in vitro* experimentation, animals were transferred 3 d after viral injection to a housing room with identical conditions and were used 3 – 6 weeks after injection. In total, 12 male C57BL/6J mice were used for intracranial pharmacological experiments, 19 male C57BL/6J mice for cardiac pharmacology experiments and 10 C57BL/6J (8 males and 2 females) mice for the fiber photometry experiments. From the DBH-Cre line, 27 (12 males and 15 females) heterozygous Cre ± animals were used for optogenetic experiments, and 14 (2 males and 12 females) for *in vitro* experiments. All experiments were conducted in accordance with the Swiss National Institutional Guidelines on Animal Experimentation and were approved by the Swiss Cantonal Veterinary Office Committee for Animal Experimentation.

METHOD DETAILS

Viral injections

Optogenetics in vivo and in vitro

Animals were anaesthetized with ketamine (83 mg kg^{-1})/xylazine (3.5 mg kg^{-1}), kept on a thermal blanket to maintain body temperature around 37°C, and injected i.p. with carprofen (5 mg kg^{-1}) for analgesia. Mice were then head-fixed on a stereotactic frame equipped with a head adaptor for young animals (Stoelting 51925). The scalp was disinfected, injected with a mix of lidocaine (6 mg kg^{-1})/bupivacaine (2.5 mg kg^{-1}) for local anesthesia and opened with scissors exposing the desired region of the skull. For the injections, we used a thin glass pipette (5-000-1001-X, Drummond Scientific) pulled on a vertical puller (Narishige), initially filled with mineral oil, and backfilled with the virus-containing solution just prior to injection. Injections took place at an injection rate of 100 – 200 nL min^{-1}. For optogenetic stimulation experiments, 1 animal was injected with a ssAAV5/2-hEF1α-dlox-hChR2(H134R) mCherry(rev)-dlox-WPRE-hGHp(A) (titer: $9.1x10^{12}$ vg / ml, 0.8 – 1 μL; Zurich VVF) virus unilaterally in a region close to the LC. The stereotaxic coordinates were (relative to Bregma, given in mm here and throughout the rest of the STAR Methods): lateral (L) ± 1.28; antero-posterior (AP) −5.45, depth (D) −3.65, as done previously.[16] Additionally, 10 animals were injected bilaterally with the same virus (0.3 – 0.6 μL) directly into the LC (L ± 1.05; AP −5.45; D −3.06) and 4 animals were injected unilaterally in the right LC. These viral injections yielded comparable results and data were pooled. For optogenetic inhibition, all animals were injected bilaterally into the LC (0.2 – 0.35 μL) with either pAAV5-CAG-FLEX-rc[Jaws-KGC-GFP-ER2] ($7x10^{12}$ vg / ml; n = 2, Addgene), AAV8-hSyn-FLEX-Jaws-KGC-GFP-ER2 ($3.2x10^{12}$ vg / ml; n = 3, UNC Vector Core) or ssAAV-5/2-hSyn1-dlox-Jaws_KGC_EGFP_ERES(rev)-dlox-WPRE-bGHp(A)-SV40p(A) (titer: $6.4x10^{12}$ vg / ml; n = 5, VVF Zürich). For control experiments, 3 animals were injected with ssAAV5/2- hEF1α-dlox-mCherry(rev)-dlox-WPRE-hGHp(A) (titer: $7.3x10^{12}$ vg / ml, 300 nL; Zurich VVF) unilaterally in the right LC.

Fiber photometry

For the assessment of NA dynamics in the thalamus, AAV viruses (ssAAV9/2-hSyn1-GRAB_NE1h-WPRE-hGHp(A), titer: $7.2x10^{12}$ vg / ml, or ssAAV9/2-hSyn1-GRAB_NE1m-WPRE-hGHp(A), titer: $5.5x10^{12}$ vg / ml, both from VVF Zürich) containing the plasmid encoding a NA sensor (pAAV-hSyn-GRAB_NE1h, Addgene Plasmid #123309, 8 animals, or pAAV-hSyn-GRAB_NE1m, Addgene Plasmid #123308, 2 animals, respectively)[40] were injected into the thalamus (500 nL; L 2.0; AP −1.6; D −3.0). After the injections,

Please cite this article in press as: Osorio-Forero et al., Noradrenergic circuit control of non-REM sleep substates, Current Biology (2021), https://doi.org/10.1016/j.cub.2021.09.041

the incision was sutured, and the area disinfected. Animals were carefully monitored and returned to the home cage once awake and moving around. Recovery time after injections took place for a minimum of 1 week before the next surgeries. Paracetamol was given in the water for the 4 postoperative days at a concentration of 2 mg ml^{-1}.

Other surgical procedures

For *in vivo* EEG/EMG combined with local field potential (LFP) recordings, electrode implantation was as previously described.[27–29] In short, animals were anesthetized with isoflurane (1.5 – 2.5%) in a mixture of O_2 and N_2O. After analgesia (i.p. carprofen 5 mg kg^{-1}) and disinfection, animals were fixed in a Kopf stereotax and injected into the scalp with a mix of lidocaine (6 mg kg^{-1})/bupivacaine (2.5 mg kg^{-1}) and a piece of the scalp was removed after 3 – 5 min, the skull exposed and the bone scratched to improve adhesion of the head implant. Then, we drilled small craniotomies (0.3 – 0.5 mm) over left frontal and parietal bones and positioned two conventional gold-coated wire electrodes in contact with the dura mater for EEG recordings. On the contralateral (right) side, a high-impedance tungsten LFP microelectrode (10–12 MΩ, 75 μm shaft diameter, FHC) was implanted in the primary somatosensory cortex (L 3; AP −0.7; D −0.85). Additionally, as a neutral reference, a silver wire (Harvard Apparatus) was inserted into the occipital bone over the cerebellum and two gold pellets were inserted into the neck muscles for EMG recordings. All electrodes were fixed using Loctite Schnellkleber 401 glue and soldered to a multisite connector (Barrettes Connectors 1.27 mm, male connectors, Conrad).

For intracranial injection of noradrenergic antagonists, we additionally made a craniotomy over the thalamus (L 2; AP −1.60) and covered it with a silicone-based sealant (Kwik-Cast Silicone Sealant, WPI). Additionally, we glued and cemented a light-weight metal head-post (Bourgeois Mécanique SAS, Lyon, France) onto the midline skull to perform painless head-fixation during injection of noradrenergic antagonists.

For optogenetic experiments, DBH-Cre animals were implanted with custom-made optic fibers.[76] A multimode fiber (225 μm outer diameter, Thorlabs, BFL37-2000/FT200EMT) was inserted and glued (heat-curable epoxy, Precision Fiber Products, ET-353ND-16OZ) to a multimode ceramic zirconia ferrule (Precision Fiber Products, MM-FER2007C-2300). The penetrating end was cut at the desired length with a carbide-tip fiber optic scribe (Precision Fiber Products, M1-46124). The outside end was then polished using fiber-polishing films (Thorlabs). For optogenetic stimulation of the LC cell bodies (n = 14 animals) a single 3-mm-long fiber stub was implanted directly over the LC (L 1.0; AP −5.4; D −2.3). Out of the 14 animals, 6 animals were also implanted with a 3 mm-optic fiber stub over the somatosensory thalamus (L 2.0; AP −1.7; D −2.5). For 5 additional animals, we implanted a custom-made optrode in S1 built with a high-impedance fine tungsten LFP microelectrodes (10 – 12 MΩ, 75 μm shaft diameter, FHC) glued to the stub of a 2 mm-optic fiber at a distance of 800 – 1,200 μm. The optrode was then inserted into S1 (L 3.0; AP −0.7; D −0.8). In the 3 additional animals, the optic fiber was not glued to the electrode but instead inserted into S1 (L 2.8; AP −0.7; D −0.3 to −0.4), while the LFP electrode was positioned at an angle of 40° below the optic fiber (L 3.0; AP −0.7; D −0.5 to −0.6). In this way, we ensured more intense illumination of the deep-layer LC fibers surrounding the LFP electrode. For optogenetic inhibition of the LC bodies (n = 10), bilateral optic fibers were implanted at a 20° lateral angle targeting the LC (L ± 1.84; AP −5.4; D −2.47). To establish the final coordinates of the optic fibers, pupil diameter changes were monitored in a subgroup of 5 animals while lowering the optic fiber and applying light stimuli (Figure S4; 10 – 30 pulses at 10 Hz). A custom-made software developed in MATLAB was used for image acquisition and data analysis (See In vivo data analysis).

For fiber photometry experiments, in addition to the recording electrodes, we implanted C57BL/6J animals (n = 10) with a premade 400 μm-thick optic fiber coupled to a cannula (MFC_400/430-0.66_3.5mm_ZF1 25(G)_FLT, Doris Lenses) over the dorsal and reticular thalamus (L 1.8; AP −1.7; D −2.5) at a speed of 1 mm min^{-1}.

Finally, a dental cement structure was built to fix the implant in place. After disinfection with iodine-based cream, animals were returned to their home cage and kept in careful monitoring. Animals were provided with paracetamol (2 mg mL^{-1}) in the drinking water for at least 4 days after the procedure.

In vivo electrophysiological recordings

Once recovered from the surgery, animals were habituated to the cabling for 5 – 7 days, followed by a baseline recording to ascertain the quality of the signals. We acquired the EEG, EMG and LFP signals at a 1 kHz sampling frequency using an Intan digital RHD2132 amplifier board and a RHD2000 USB Interface board (Intan Technologies) connected via SPI cables (RHD recording system, Intan Technologies). Homemade adapters containing an Omnetics - A79022-001 connector (Omnetics Connector) linked to a female Barrettes Connector (Conrad) were used as an intermediate between the head implant of the animal and the headstage. We acquired the data with MATLAB using the RHD2000 MATLAB toolbox and a customized software in the same environment.[27,28]

Procedures for intracranial pharmacology

We gently and gradually habituated mice to being head-fixed by increasing the amount of time spent in head fixation daily from 5 min to 45 min over a period of 4 – 5 days. The rest of the time, the animals spent being tethered to the recording system in their home cage. On the first experimental day, we removed the silicone cover of the craniotomy in head-fixed conditions and positioned a glass pipette (5-000-1001-X, Drummond Scientific, pulled on a vertical Narishige PP-830 puller, tip size of 15 – 25 μm) over the craniotomy and waited for 30 min while gently touching the side of the craniotomy to simulate an injection. Then, we covered the craniotomy again with the silicone-based sealant and returned the animals to the home cage for an 8 h-baseline polysomnographic recording. The next day, we removed the silicone again and injected 150 nL of noradrenergic antagonists or ACSF at two different depths within the thalamus (D: −3.2 and −2.8 mm). For the experimental group, we infused a mixture of 0.1 mM prazosin hydrochloride (prazosin)

Please cite this article in press as: Osorio-Forero et al., Noradrenergic circuit control of non-REM sleep substates, Current Biology (2021), https://doi.org/10.1016/j.cub.2021.09.041

and 5 mM (S)-(-)-atenolol (atenolol), diluted in ACSF together with a red fluorescent dye (5 mM Alexa 594) for later confirmation of the injection site. For the control group, we injected ACSF together with Alexa 594. Per animal, only one injection was done (either blockers or ACSF) and the animal sacrificed after completion of the recording.

Procedures for *in vivo* optogenetics

All optogenetic manipulation took place during the first 20 min of each hour between ZT1 and ZT9. A custom-made close-loop detection of NREMS[28] was used for state specificity. In short, NREMS was detected whenever the delta (1 – 4 Hz) to theta (5 – 10 Hz) power ratio derived from the differential frontal-parietal EEG channels crossed a threshold for 2 out of 5 s and the EMG absolute values went below a threshold during at least 3 s. This lead to reliable stimulation during NREMS (Figure 2), with the exception of a few brief interruptions that occurred during artifacts (e.g., muscle twitches). Stimulation sessions took place in the first 20 min of each hour during 8 h of the light phase (ZT1-9), with light or sham (light source turned off) stimulation alternating over successive recording days. Optogenetic stimulation of the LC cell bodies was carried out using a PlexBright Optogenetic Stimulation System (Plexon) coupled to a PlexBright Table-top blue LED Module (Wavelength 465 nm) at 1 Hz (light intensity of 2.8 – 3.2 mW at the tip). Stimulation of LC terminals in the thalamus or cortex was delivered at 2 Hz (Figure 3). Optogenetic inhibition of LC cell bodies was performed using a continuous stimulation with a PlexBright Table-top orange LED Module (Wavelength 620 nm, light intensity 1.55 – 1.7 mW at the tip) (Figure 2). Optogenetic stimulation (1 Hz) or inhibition (continuous) was also carried out specifically when sigma power declined or rose. This was achieved via a machine-learning-based closed-loop procedure[27] built with a multilayer perceptron model neural network of 10 neurons in the hidden layer and 3 output neurons (for rising or decreasing sigma power during NREM or to no stimulation, in the case of epochs outside this sleep state). The network was fed with the last 200 s of a 9^{th}-order polynomial fit of the sigma activity (10 – 15 Hz) calculated for each s. The neural network was then trained, validated, and tested using the sleep scoring from 13 C57BL/6J animals (642,000 epochs) that were otherwise not included in this study. Online, the same data stretches obtained from the mouse in recording were used.

For each animal, multiple recording sessions took place with a random allocation of the stimulation protocol: i.e., optogenetic stimulation during NREMS in the LC bodies, its terminals (thalamus for 6 animals or cortex 8 animals), or stimulation of the LC bodies during spindle-enriched or -poor substates (in a subgroup of 9 mice). Similarly, for optogenetic inhibition of LC bodies, random allocation of inhibition protocols took place during NREMS (10 animals) or NREMS substates (10 animals).

Procedures for *in vivo* fiber photometry

After the recovery (> 7 d) and habituation to the cabling procedure (> 4 d), we performed two recordings per animal with at least one day between sessions. All recordings were limited to the first 3 – 4 h from ZT1 to minimize possible photobleaching. For fluorescent measurements, we used a pulse-width-modulated sinusoidal signal of 400 Hz using a Raspberry Pi3 (Raspberry Pi Foundation) to modulate a LEDD_2 driver (Doric Lenses) connected to a blue LED (CLED 465 nm; Doric Lenses). The power of the driver was set to 200 mA. The blue LED was coupled to a fluorescence MiniCube (iFMC4_IE(400-410)_E(E460-490)_F(500-550)_S, Doric Lenses) that redirected the light to the animal via a low autofluorescence 400-μm-thick fiberoptic patchcord (MFP_400/430/1100-0.57_1m_FMC-ZF1.25_LAF, Doric Lenses). The cord was connected to the Optic fiberoptic Cannula (MFC_400/430-0.57_3mm_ZF1.25(G)_FLT) implanted in the head of the mouse. A photodetector integrated into the MiniCube head turned the emitted light from the fluorescent NA sensor into a current signal that was fed into an analog signal of the Intan RHD2132 amplifier board. To ensure that data collected were within the dynamic range of the biosensors, awake animals were exposed to the experimenter's hand held within the cage for 1 min moving gently but without touching the animal (Figure S6).

In vitro electrophysiological recordings

Thalamic brain slice recordings were performed as previously described in detail.[29,76] Briefly, 3 – 6 weeks after viral injection, DBH-Cre mice aged 8 – 16 weeks were subjected to isoflurane anesthesia, after which they were decapitated, brains extracted and quickly immersed in ice-cold oxygenated sucrose solution (which contained in mM): NaCl 66, KCl 2.5, NaH_2PO_4 1.25, $NaHCO_3$ 26, D-saccharose 105, D-glucose 27, L(+)-ascorbic acid 1.7, $CaCl_2$ 0.5 and $MgCl_2$ 7), using a sliding vibratome (Histocom). Brains were trimmed at the level of the brainstem, glued on the trimmed surface on an ice-cold metal blade and apposed to a supporting agar block on their ventral side. Acute 300-μm-thick coronal brain slices were prepared in the same ice-cold oxygenated sucrose solution and kept for 30 min in a recovery solution at 35°C (in mM: NaCl 131, KCl 2.5, NaH_2PO_4 1.25, $NaHCO_3$ 26, D-glucose 20, L(+)-ascorbic acid 1.7, $CaCl_2$ 2, $MgCl_2$ 1.2, *myo*-inositol 3, pyruvate 2) before being transferred to room temperature for at least 30 min. All recordings were done at room temperature.

Recording glass pipettes were pulled from borosilicate glass (TW150F-4) (WPI) with a DMZ horizontal puller (Zeitz Instr.) to a final resistance of 2 – 4 MΩ. Pipettes were filled with a K^+-based intracellular solution that contained in mM: KGluconate 140, HEPES 10, KCl 10, EGTA 0.1, phosphocreatine 10, Mg-ATP 4, Na-GTP 0.4, pH 7.3, 290–305 mOsm. Slices were placed in the recording chamber of an upright microscope (Olympus BX50WI) and continuously superfused with oxygenated ACSF containing in mM: NaCl 131, KCl 2.5, NaH_2PO_4 1.25, $NaHCO_3$ 26, D-glucose 20, L(+)-ascorbic acid 1.7, $CaCl_2$ 2 and $MgCl_2$ 1.2. Cells were visualized with differential interference contrast optics and 10X and 40X immersion objectives, and their location within the thalamic ventroposterial medial nucleus or within the somatosensory reticular thalamus could be verified based on previous studies in the lab.[29,76] Infrared images were acquired with an iXon Camera X2481 (Andor). Prior to recording, pipette offset was zeroed, and the stability of the offset verified by monitoring pipette potential in the bath for 10 min. Drifts were < 0.5 mV / 10 min. Signals were amplified using a Multiclamp

Please cite this article in press as: Osorio-Forero et al., Noradrenergic circuit control of non-REM sleep substates, Current Biology (2021), https://doi.org/10.1016/j.cub.2021.09.041

700B amplifier, digitized via a Digidata1322A and sampled at 10 kHz with Clampex10.2 (Molecular Devices). Immediately after gaining whole-cell access, cellular membrane potential and access resistance were measured. Cells included had a resting membrane potential < −55 mV and access resistances < 15 MΩ. The cell types were identified based on their rebound bursting properties (Figure S7). Whole-field blue LED (Cairn Res) stimulation (455 or 470 nm, duration: 0.1 – 1 ms, maximal light intensity 0.16 and 0.75 mW/mm^2 for the two LEDs, respectively). Per slice, only one cell was recorded and exposed to light stimulation. For characterization of LC fiber-evoked membrane depolarizations, cells were held between −65 to −70 mV and exposed to 1 Hz, 3 Hz or 10 Hz stimulation (4 pulses each, of 100 μs). Stimulation at different frequencies were applied in random order, with each frequency used maximally twice to avoid run-down of the evoked response. When light-induced depolarizations did not return to the original membrane potential, they were not included in the analysis. For the study of LC-dependent effects on prolonged afterdepolarizations, thalamocortical cells were first injected with series of repetitive negative current injections (100 – 300 pA, 20 pulses, each 120 ms) known to evoke rebound low-threshold Ca^{2+} bursts. Such protocols have been used previously to characterize the cell-intrinsic mechanisms accompanying sleep-spindle-related arrival of barrages of inhibitory synaptic potentials.[43] Following 1 – 2 such repetitive current injections (each followed by 3 – 5 min of recovery time), the current injections were preceded by LC fiber stimulation (10 Hz, 4 pulses) by 5 s, such that the maximum of the LC-evoked membrane depolarization coincided with the end of the negative current injections. For characterization of LC fiber-evoked membrane currents, cells were held in voltage-clamp at −70 mV. Baseline light-evoked currents were evoked maximally 1 – 2 times, followed by bath application of cesium chloride or noradrenergic antagonists ((S)-(-)-atenolol (Abcam) for thalamocortical cells or prazosin hydrochloride (Abcam) for thalamic reticular cells) for 5 – 10 min before the next optogenetic stimulation. The *in vitro* data were manually analyzed using Clampfit v2.2 and as illustrated in Figure S7.

Pharmacological manipulation of heart rate

After the recovery period of the electrode implantation (> 7 d), mice were habituated to the recording conditions for one week. Mice were injected intraperitoneally with NaCl, (S)-(-)-atenolol (1 mg kg^{-1}) (Abcam), a sympathetic antagonist or methylatropine bromide (10 mg kg^{-1}) (Sigma-Aldrich), a parasympathetic antagonist, both known to poorly permeate the blood-brain barrier.[44,45] Injections were done at 9 am and followed by polysomnographic recording for 100 min. Two recording sessions per drug took place in an intercalated manner. Experimenters were blind to the drug injected.

Histology

After all recording sessions were completed, animals were injected intraperitoneally with a lethal dose of pentobarbital. For animals implanted with electrodes for LFP recording, the position of the electrode was marked via electro-coagulation (50 μA, 8 – 10 s) of the region. Subsequently, ∼45 mL of paraformaldehyde (PFA) 4% were perfused intracardially at a rate of ∼2.5 mL min^{-1}. Brains were post-fixed for at least 24 h in PFA 4% cooled to 4°C. Brains were then sliced in 100 μm-thick sections with a vibratome (Microtome Leica VT1000 S; speed: 0.25 – 0.5 mm s^{-1} and knife sectioning frequency: 65 Hz) or a freezing microtome (Microm). Brain sections were directly mounted on slides or kept in well plates filled with 0.1 M PB for later processing. Then, we confirmed the position of LFP electrodes and optic fibers and the fluorescent expression of the injected viruses or local pharmacology injections with a Nikon SMZ25 Stereomicroscope equipped with a Nikon DS-Ri2 16 Mpx color camera. When needed, higher magnification images were acquired using an Axiovision Imager Z1 (Zeiss) microscope equipped with an AxioCam MRc5 camera (objectives used EC-Plan Neofluar 2.5x/0.075 ∞/0.17, 5x/0.16 ∞/0.17, 10x/0.3 ∞/- or 20x/0.5 ∞/0.17).

For quantification of TH-expressing neurons and the fraction of ChR2_mCherry neurons, 50-μm slices (coronal, ∼5.3 mm from bregma) were washed 3 times in PBS and 0.3% Triton, followed by a 1-h incubation in a blocking solution of PBS 0,3% Triton and 2% normal goat serum. Next, overnight incubation of the sections in the primary antibody was performed at 4°C on a shaking platform with a dilution of 1:2000 mouse anti-TH antibody (Immunostar, 22941) as primary antibody in the same blocking solution. After at least 12 h, slices were washed 3 times in PBS and 0.3% Triton, followed by a 1 – 1.5 h incubation with 1:150 goat anti-mouse antibody coupled to Alexa Fluor 488 (Invitrogene, A32723) as secondary antibody (in a PBS and 0.3%Triton, at room temperature) on a shaking platform. After immunostaining, slices were rinsed with PB 0.1 M and mounted on slides with Moviol as mounting medium. For visualization of ChR2_mCherry-expressing fibers in thalamus and cortex, an immunostaining enhancement of the mCherry fluorophore was performed using a procedure similar to the one for staining LC cell bodies, using 1:500 Rabbit polyclonal Anti-mCherry antibody (abcam, Ab183628) and 1:300 donkey anti-rabbit Alexa Fluor 594 antibody (Invitrogen, R37119) as primary and secondary antibodies respectively.

QUANTIFICATION AND STATISTICAL ANALYSIS

In vivo data analysis

Scoring of vigilance states

Using EEG/EMG data, we detected sleep and wake episodes following previous standard procedures in a manner blinded to the treatment. For this purpose, we used a custom-made software developed in MATLAB (MathWorks) that allows semiautomatic scoring of sleep stages.[27,28] Shortly, we defined three distinct stages as follows: wakefulness, periods containing large muscle tonus or phasic activity in the EMG signal, together with low-voltage EEG exhibiting fast oscillatory components. NREMS was defined as periods containing low EMG activity together with high amplitude EEG activity showing slow oscillatory components such as slow oscillations (< 1.5 Hz), delta (1.5 – 4 Hz) or sleep spindles (10 – 15 Hz). REMS episodes were defined as periods with low EMG activity

Please cite this article in press as: Osorio-Forero et al., Noradrenergic circuit control of non-REM sleep substates, Current Biology (2021), https://doi.org/10.1016/j.cub.2021.09.041

CellPress
OPEN ACCESS

with prominent Theta (5 – 10 Hz) activity in the EEG. Microarousals were defined as short (< 12 s) periods of wakefulness contained between the epochs of the same sleep stage. Quiet wakefulness (QW) studied in Figure 5 was distinguished from active wakefulness based on EMG, as illustrated in Figure S5 and as published.[28] For the intracranial pharmacology experiments, analysis was done for the first 2 h of recording and comparisons were made in a paired manner between the baseline and drug conditions. For all optogenetic experiments, scored data for the first 20 min of each hour (during which light stimulation was done) were compared with the same periods in sham conditions (*ceteris paribus* with the LED turned off). For the fiber photometry experiments, analysis included the complete 3 – 4 h of recordings. For the pharmacological manipulation of the HR, analysis took place for the first 100 min after the i.p. injections.

Analysis of sigma and delta dynamics

Throughout the study, all analyses of spectral dynamics, in particular within the sigma (10 – 15 Hz) and delta (1.5 – 4 Hz) bands, were quantified from the either the S1 LFP or EEG signal using a wavelet transform with a Mother Gabor-Morlet wavelet with 4 cycles of standard deviation for the Gaussian envelope (Figures 1A and 1C). The frequency dimensions were then collapsed to the two frequency bands of interest, the 10 – 15 Hz sigma band and the 1.5 – 4 Hz delta band. The mean signals were then resampled at 10 Hz and filtered using a 100^{th} order filter with a 0.025 Hz cutoff frequency for further analysis. For NREMS bouts of $\geq$ 96 s, a Fast Fourier transform was calculated (Figure 1B) to measure the strength of the 0.02 Hz oscillatory patterns defined here as the area underneath the Fourier transform from 0.01 – 0.04 Hz, subtracting the mean activity between 0.08 to 0.12 Hz (as depicted in Figure 1B). For the example depicted in Figure 1B, the sigma and delta grand averages were calculated from the long bouts (> 96 s) of NREMS of baseline recordings contained within ZT1-7 (local pharmacology experiment) or ZT1-9 (optogenetic experiments).

Sleep spindle detection, phase coupling analysis and feature extraction

Sleep spindles were detected from the S1 LFP signal for all the experiments. Spindle detection was done using a previously described algorithm[29] that is illustrated in Figure S1. Briefly, we filtered (FIR filter of order 2000) the raw S1 LFP signal in a wide sigma band (9 – 16 Hz). Then, we squared the signal and applied a threshold of 1.5 the standard deviation above the mean values in NREMS. We then detected all the peaks crossing this threshold and marked as a putative spindle all events containing at least 3 cycles. The starting and ending point of the events were extended to the closest cycle at 0 crossing before and after the threshold, respectively. Events separated by < 50 ms were merged as a single event. For display purposes, we positioned a black dot for each individual spindle event at the center of the spindle in time and a random jittered vertical position.

After spindle detection, we extracted the following features: *Amplitude,* the maximum value of the absolute filtered signal within the event. *Frequency,* mean intra-peak frequency within the detected spindle event. *Number of cycles* in the spindle. *Duration,* time span between the beginning and end of the event.

For the analysis of the phase coupling of the spindle events to the sigma activity we first centered the sigma activity at zero by subtracting the mean of the sigma activity in NREMS. Then we constructed a distribution using the phase of the sigma dynamics (calculated as described in Analysis of sigma and delta dynamics) at the center of each spindle event (half point between the beginning and the end of the spindle). By using the CircStat toolbox for MATLAB (MathWorks),[71] we then confirmed the non-uniformity of the distribution by using the Rayleigh test.

Detection of infraslow cycles

We detected individual cycles of sigma within NREMS using a custom-made MATLAB routine. We used the sigma dynamics as described in Analysis of sigma and delta dynamics and eliminated the regions containing artifacts. Then, we identified the peaks and troughs in the signal with a minimum distance of 25 and 20 s, respectively. Finally, we arranged the positions of successive troughs and kept the starting and ending point for each individual cycle. Next, the marked locations were used to normalize the time in 1000 points for each individual cycle and to interpolate the sigma activity to generate a mean dynamics normalized in time. The same positions were used to normalize the dynamics of NA-related fluorescent signals from the fiber photometry measurements. Only those cycles that within NREMS periods were included in the mean.

Pupil diameter measurements

To standardize the correct location of the optic fibers in the LC cell bodies stimulation or inhibition, we performed pupil diameter measurements in a subset of animals. In short, we set a Basler GigE infrared camera (Basler acA800-510 um, SVGA, 1/3.6'', 510 fps, USB3 Vision) close to one eye of the animal and used a custom-made infrared LED-based lantern directed to the recorded eye to increase the contrast between the pupil and the surrounded area. We built a custom-made software in MATLAB (MathWorks) for online or offline pupil detection (using the videos recorded from online trials). First, the user manually selects both the area of interest for the analysis and the initial location of the pupil. Then, for each frame (recorded at 10 fps), a binary image was created using an Otsu's method adaptive threshold with the function imbinarize from MATLAB (MathWorks). The threshold was set manually to adapt to the conditions of the image and the angles of the infrared light source and the camera. The size of the binary object closest to the marked pupil was then measured. The dynamics of the pupil diameter was then tracked and z-scored for comparison (Figure S4).

Fiber Photometry

Changes in bioluminescence were recorded via a photodetector connected to an analog channel in the Intan RHD2000 USB Interface board (Intan Technologies) as described before. The recorded signal fluctuated between 0 – 3.3 V with peaks at 400 Hz as the sinusoidal waveform created to modulate the excitation of the biosensors. The fluorescent dynamics signal was then created using an RMS envelope of 1 s. The changes in biofluorescence $\Delta F * F^{-1}$ were computed by dividing the enveloped signal by its fitted exponential decrease calculated from the dynamics at NREMS. We computed the relative fluorescence across different sleep states using the z-scored data per recording session; using the mean values across all vigilance states for the z-scoring. The values presented in

Please cite this article in press as: Osorio-Forero et al., Noradrenergic circuit control of non-REM sleep substates, Current Biology (2021), https://doi.org/10.1016/j.cub.2021.09.041

Figure 5B and in Figure S5 show the mean values of multiple sessions per animal for quiet wakefulness (QW), NREM (NR) and REM (R) sleep. In every case, only epochs flanked by epochs of the same vigilance state were included.

Cross correlation analysis

To study the similarity of the dynamics between the sigma activity and the NA changes or changes in HR, we performed cross correlation analysis between these two pairs of signals in MATLAB (MathWorks). For each long bout ($\geq$96 s) of NREMS within the time of analysis (see Scoring of vigilance states), we z-scored each signal individually and normalized it to the length of the bout. Then, the cross-correlation was calculated using the function xcorr of MATLAB and normalized to the length of the bout. Mean cross correlation values were computed for each animal and across animals. Mean correlation coefficient (r) was computed between -5 to 5 s lags.

Heart rate analysis

Changes in HR were computed as previously described.[27] Shortly, EMG signal was filtered using a Chebyshev type 2 high-pass filter. We then differentiated (using the function diff from MATLAB) and squared the signal to highlight the R peaks. The resulting signal was z-scored to normalize across animals and recording sessions. Then, the R peaks were identified using the MATLAB function findpeaks with a heuristically found threshold of 0.3 and an interpeak distance of at least 0.08 ms. Peaks with a z-score higher than 10 were considered as artifacts and eliminated. Finally, the HR signal was constructed by measuring the inter-peak time distance and divided by 60 (1 min). An interpolation of the values was performed using the function interp1 of MATLAB and resampled at 10 Hz.

Histological analysis

The efficiency and specificity of expression of viral transgenes was done by quantifying the overlap between TH- and mCherry-expressing neurons. Total cell counts were obtained from two 50-μm-thick sections per mouse containing LC around Bregma -5.3 using spinning disk confocal microsocopy (Nikon Ti2, CrEST Optics X-Light V3). Per mouse, 100 – 279 TH-expressing and 100 – 214 mCherry-expressing cells were counted in separate green and red fluorescent channels. For quantifying the overlay, single-focal-plane pictures were used to count separately the green-only, red-only and the yellow cell bodies. Percentages were calculated with respect to the total cell count. Per animal, 67 – 190 cells were counted.

To assess the fiber density within the stimulation areas within the thalamus and the somatosensory cortex we performed an immunostaining enhancement of the mCherry fluorophore from the ChR2 expressing terminals as described before (Histology). From 100 μm-thick sections containing the VPM or the S1 cortex (-1.7 mm and -0.7 mm from bregma, respectively), we took Multilayer Z stack pictures using a tile scan of 5x5 with a magnification of 40x (CFI Plan Apochromat Lambda 40XC N.A. 0.95, W.D. 0.21 mm, Spring-loaded, Cover glass correction: 0.11 – 0.23 mm). For latter analysis we used ImageJ (https://imagej.nih.gov/ij/). An area of 0.13 mm^2 was then randomly selected within the VPM and S1 around the stimulation optic fiber. Then a background subtraction with a 3 pixel-rolling radius was performed, then we performed a contrast enhancement with a saturation of 0.35 and a mask was created with a median radius of 2 pixels. From the resultant binary image, we quantified the area of the positive (bright) pixels within the window (Figure 3C).

Statistical analysis

For the statistical tests, we used R statistical language version 3.6.1. and MATLAB (MathWorks). First, we tested for normality of the datasets using the Shapiro-Wilk normality test. For comparisons of two parametric datasets, we used a paired Student's t test and the equivalent Wilcoxon signed rank test for non-parametric datasets. For comparisons on multiple (> 2) groups of data (as in the case of the amplitude, onset latency and recovery time in the in-vitro experiments), a one-way ANOVA or a Kruskal-Wallis test was used for parametric and non-parametric datasets, respectively. F and χ^2 indicated in the figures are derived from ANOVA and Kruskal-Wallis tests, respectively. In case of no significance, no further post hoc analysis was performed. In all figures, gray lines denote paired datasets from two conditions (e.g., baseline, opto). Mean values are given by large horizontal lines, error bars indicate standard errors of the mean. Throughout the figures, V, t and p values were derived from Wilcoxon signed rank or paired t tests, respectively.